1   **Deforestation as an anthropogenic driver of mercury pollution**

2

3   Aryeh Feinberg[a], Martin Jiskra[b], Pasquale Borrelli[c], Jagannath Biswakarma[b,d], and Noelle E.

4   Selin[a,e]

5

6   [a] *Institute for Data, Systems, and Society, Massachusetts Institute of Technology, Cambridge,*

7   *MA, USA*

8   [b] *Environmental Geosciences, University of Basel, Basel, Switzerland*

9   [c] *Department of Science, Roma Tre University, Rome, Italy*

10   [d] *Department of Water Resources and Drinking Water, Eawag, Dübendorf, Switzerland*

11   [e] *Department of Earth, Atmospheric, and Planetary Sciences, Massachusetts Institute of*

12   *Technology, Cambridge, MA, USA*

13   Correspondence to: arifeinberg@gmail.com (A.F.); martin.jiskra@gmail.com (M.J.)

14

15   **Abstract**

16   Mercury (Hg) released by anthropogenic activities can bioaccumulate to neurotoxic levels in

17   commonly consumed fish. Soils are a global long-term storage for atmospheric Hg taken up

18   by vegetation, thereby decreasing the Hg burden to oceans and eventually fish. Deforestation

19   reduces the capacity of the terrestrial Hg sink and enhances the release of Hg from soils.

20   However, the consequences of deforestation on Hg cycling are not currently considered by

21   anthropogenic emissions inventories or specifically addressed under the global Minamata

22   Convention on Mercury. Here, we use global Hg modeling constrained by field observations

23   to quantify the impact of forest cover changes on the Hg cycle. We estimate that atmospheric

24   Hg fluxes due to deforestation are 217 Mg yr^{-1} (95% confidence interval, CI: 134–1650 Mg

25   yr^{-1}) for 2015, approximately 10% of global primary anthropogenic emissions. We calculate

26   the potential for substantial Hg emissions reductions for two cases of land use policies:

27   conservation of the Amazon rainforest (92 Mg yr^{-1}, CI: 59 to 234 Mg yr^{-1}) and global

28   reforestation (98 Mg yr^{-1}, CI: 64 to 449 Mg yr^{-1}). This study shows that deforestation is an

29   overlooked source in anthropogenic Hg emissions inventories and illustrates the potential

30   benefits of land use policy to address global Hg pollution.

Introduction

Humans are exposed to the organic form of mercury (Hg), methylmercury (MeHg) through fish and seafood consumption[1]. Methylmercury is a potent neurotoxin, impairing the neurodevelopment of fetuses and children and costing the global economy $20–117 billion annually according to some estimates[32,3]. Mercury is emitted to the atmosphere by 1) primary anthropogenic sources, including artisanal and small-scale gold mining (ASGM), fossil fuel combustion, and metal smelting; 2) re-emissions of historical anthropogenic ("legacy") Hg from ocean and land; and 3) geogenic sources[4]. Mercury spreads globally in the atmosphere due to its long lifetime of 4–6 months[5]. A global treaty, the Minamata Convention on Mercury, aims to protect human health and the environment from anthropogenic emissions and releases of Hg. Its measures target primary anthropogenic emissions sources by phasing out Hg use and adopting best available technologies for pollution control[6]. However, primary anthropogenic emissions account for only 30% of present-day total emissions, with legacy re-emissions from land and ocean accounting for 60%[7]. The future of Hg pollution will depend not only on reducing direct emissions through the Minamata Convention, but also on indirect anthropogenic influences on legacy Hg emissions and fate.

Terrestrial ecosystems, and especially forests, are important sinks of Hg from the atmosphere, taking up an estimated 2200–3600 Mg Hg per year[8], more than a third of total (anthropogenic, legacy, and geogenic) Hg emissions (7400 Mg yr^{-1})[9]. By taking up Hg, terrestrial ecosystems reduce the burden of Hg depositing in oceans, where it can be converted to MeHg and bioaccumulated in fish. Previous studies have drawn useful analogies between Hg and carbon cycling in terrestrial ecosystems[10,11]. Like carbon dioxide (CO_2), elemental mercury (Hg^0) is assimilated by foliage throughout the growing season[12]. Mercury is transported from the canopy to soil by foliage falling to the ground ("litterfall") and being washed off by precipitation ("throughfall"), which together are the major source (60–90%) of Hg in soils[8]. Anthropogenic land use and land cover changes (LULCC), including deforestation, perturb both CO_2 and Hg fluxes to the atmosphere[13–15]. In the case of carbon, scientific assessments have calculated the contribution of LULCC to total CO_2 emissions (13% of total[14]), and land management practices are governed by Article 5 of the Paris Agreement[16]. For Hg, on the other hand, quantitative information related to the overall importance of land cover change is limited. Only one previous study modeled the impact of future LULCC on atmospheric Hg cycling, focusing on the effects of climate-induced changes to vegetation[15]. No anthropogenic Hg emissions inventories have quantified the impacts of historical and future deforestation, and land management is not currently addressed by Hg policy efforts like the Minamata Convention.

Several processes mobilize Hg from terrestrial systems after deforestation. Along with removing a strong atmospheric sink of Hg, deforestation leads to more insolation reaching the soil, increasing photo-reduction and volatilization of Hg from soils[17]. Fire-mediated deforestation leads to direct emission of Hg from forest and soil biomass[18]. Soils in deforested areas are subject to accelerated erosion rates, enhancing Hg export to downstream ecosystems[19–21]. Direct measurement of deforestation-driven fluxes at larger scales is challenging given variations in the land sink due to trends in environmental conditions, necessitating the use of models to quantify these fluxes[22]. Models of terrestrial–atmosphere Hg fluxes, while still being much more uncertain than similar carbon cycle models, are improving due to a better process understanding and increasing availability of terrestrial measurements[8,12,23,24]. Thus, the time is ripe for assessing the relative importance of deforestation-driven fluxes in the Hg cycle.

Policies on local, national, and international scales will shape the future evolution of deforestation Hg fluxes. Deforestation due to agricultural land conversion threatens the Amazon rainforest[25,26], which currently contributes 29% of the global land sink for atmospheric Hg^0 (ref.[23]). At current deforestation rates, 40% of the Amazon rainforest could be lost by 2050, while enhanced environmental legislation (e.g., expansion of protected areas and enforcement) can reduce the deforested area to 15%[27]. Reforestation and afforestation on the global scale are being studied as part of the solution to reach net zero greenhouse gas emissions in the future[28], though the efficacy of these measures has been debated[29,30]. In any case, the climate mitigation benefits of forestation would not be realized without accompanying aggressive CO_2 emissions reductions[29,31]. Similarly, forest conservation and reforestation policies may have potential benefits for Hg sequestration on land, yet the magnitude of impacts remain unquantified.

Here, we apply the GEOS-Chem Hg model[23] to calculate deforestation emission factors for Hg from different regions and evaluate them against available observations. We quantify the global atmospheric Hg fluxes in 2015 that result from deforestation (217 Mg yr^{-1}; 95% confidence interval, CI: 134–1650 Mg yr^{-1}). We study the impact of future Amazon deforestation policy scenarios[27] and potential global reforestation efforts[31] on the terrestrial Hg sink. The magnitude of potential emissions reductions from Amazon conservation (92 Mg yr^{-1}; CI: 59–234 Mg yr^{-1}) and global reforestation (98 Mg yr^{-1}; CI: 64–449 Mg yr^{-1}) highlights the importance of land management policies for curbing Hg pollution.

99 **Global estimate of deforestation-driven Hg fluxes**

100 In quantifying changes to Hg fluxes after deforestation, we define the net deforestation

101 emissions as the change in the net terrestrial-atmosphere exchange (emissions minus

102 deposition) over a deforested area. For our global estimate of deforestation-driven emissions,

103 we do not consider immediate biomass burning emissions of Hg due to fire-mediated forest

104 clearing, rather looking at the impact on net Hg fluxes to the atmosphere in the years after the

105 clearing event. The major impacts to Hg fluxes arise through enhanced soil Hg^0 emissions and

106 decreased Hg^0 dry deposition, which can continue many years after the initial deforestation

107 event[17,32]. Using perturbation simulations in GEOS-Chem for 8 global land regions, we

108 calculated regional emission factors (EFs) representing net fluxes to the atmosphere per unit

109 area that is deforested (in units Mg Hg m^{-2} yr^{-1}). The calculated EFs are on the order of 10^{-6} to

110 10^{-4} Mg Hg m^{-2} yr^{-1} depending on the region (Fig. S4; Table S3), with the Amazon rainforest

111 showing the highest EF (7×10^{-5} Mg Hg m^{-2} yr^{-1}; CI: 4×10^{-5} to 2×10^{-4} Mg Hg m^{-2} yr^{-1}).

112 This is to be expected from litterfall and throughfall measurements in the Amazon, which

113 show some of the highest levels of Hg^0 vegetation uptake observed globally[13], as well as Hg^0

114 soil flux measurements from deforested areas in the Amazon, which show higher levels of

115 emissions in compared to deforested North American soils[17]. We compiled available

116 estimates of deforestation EFs from previous observational studies[17,20,24,32–48] and compare

117 these to our modeled values (Fig. S4). Our EFs overlap with available factors derived from

118 observations, for the three regions where these are available (Amazon, China, and Nearctic).

119 We multiply the regional EFs by the deforested area from the CMIP6 Land-Use

120 Harmonization (LUH2) dataset[49] to calculate the net Hg fluxes to the atmosphere from

121 deforestation. Given the uncertain timescale for recovery in Hg sink capacity after

122 deforestation, we assume that a deforested area has constant annual emissions over a

123 considered time horizon. Previous LULCC studies for carbon suggest that forests recover

124 their original biomass within 75 years after deforestation[50], so we employed time horizons

125 between 15–60 years (Fig. S7) to calculate 2015 deforestation-driven emissions. In Fig. 1a,

126 we present country-level deforestation emissions based on a 45-year time horizon (emissions

127 released from areas deforested between 1970 and 2014). Net emissions occurring in 2015

128 considering this 45-year deforestation time horizon are 217 Mg yr^{-1} globally (CI: 134–1650

129 Mg yr^{-1}). Countries with substantial (>10 Mg yr^{-1}) deforestation-driven emissions include

130 Brazil (43 Mg yr^{-1}), Indonesia (35 Mg yr^{-1}), China (16 Mg yr^{-1}), Colombia (14 Mg yr^{-1}), India

131 (13 Mg yr^{-1}), Philippines (11 Mg yr^{-1}), and Myanmar (11 Mg yr^{-1}). To put these emissions

132 into context, Fig. 1b compares the deforestation emissions with 2015 primary anthropogenic

133 emissions inventory from AMAP/UNEP[9,51]. Deforestation Hg emissions are minor (<5%)

134 compared to primary anthropogenic emissions for most countries. However, for 32 countries,

135 all located in the tropics, deforestation emissions are greater than 30% of primary emissions.

136 Deforestation emissions even exceed primary emissions in some countries, including

137 Madagascar (deforestation emissions are 2.4× larger), Paraguay (2.3×), Liberia (2.0×), and

138 Bangladesh (1.8×). For Brazil, which is the fifth highest emitter of primary Hg[9,51],

139 deforestation emissions (43 Mg yr^{-1}) equate to 60% of the 2015 primary emissions (156 Mg

140 yr^{-1}). Currently, Hg emissions inventories only consider primary anthropogenic emissions

141 (2222 Mg yr^{-1} in 2015; ref. [9]), overlooking deforestation as a significant source of

142 anthropogenic Hg to the atmosphere (217 Mg yr^{-1}). The relative importance of deforestation

143 as an anthropogenic driver of Hg pollution could increase over the next decades, with primary

144 anthropogenic emissions of Hg projected to halve to 1020 Mg yr^{-1} by 2035 under Minamata

145 policies and reductions in fossil fuel use[52]. Therefore, assessing the potential impacts of land

146 policy scenarios will be crucial for predicting future Hg cycling.

147
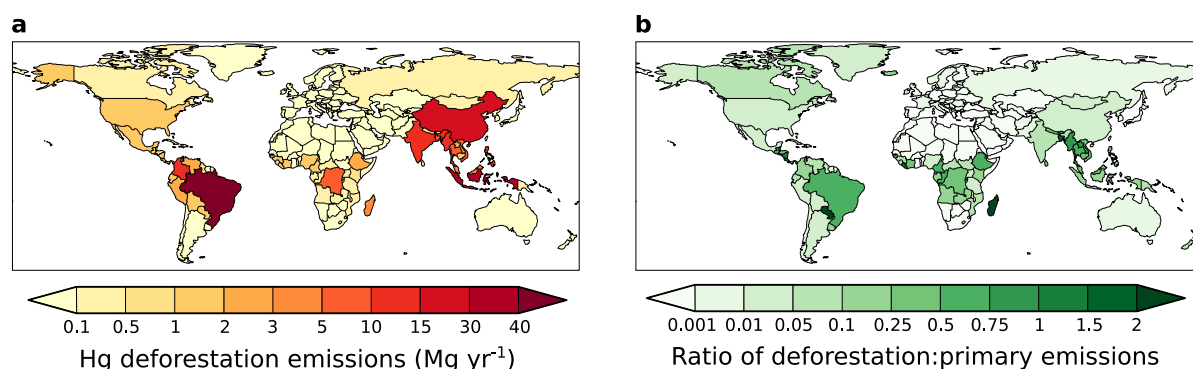
148 **Figure 1. Country-level annual deforestation emissions of Hg in 2015. a.** Deforestation-driven net
149 emissions of Hg by country, assuming that deforested areas from the previous 45 years (1970–2014)
150 contribute to emissions. **b.** Ratio of deforestation emissions to primary anthropogenic emissions[9,51] by
151 country.

152

Amazon conservation policy impacts on Hg cycling

154 The Amazon is one of the regions with the highest Hg fluxes from deforestation (Fig. 1) and

155 policy choices will determine how this evolves in the future. Under historical forest coverage

156 from 2003 (HIST simulation), the Amazon rainforest stands out as a strong global sink of Hg

157 (Fig. 2a), with net input from the atmosphere to the rainforest totalling 332 Mg yr^{-1} (CI: 179–

158 463 Mg yr^{-1}). We study the evolution of the Amazon Hg sink in two deforestation scenarios[27]

159 for 2050: a business-as-usual scenario (BAU), which extrapolates historical deforestation

160 tendencies into the future, and a governance scenario (GOV), which assumes expanded

161 conservation of the rainforest in the future. In the BAU scenario, widespread deforestation,

162 mainly in eastern Amazonia, reduces the net Hg inputs to soils (Fig. 2b). The removed

163   vegetation leads to decreased Hg^0 deposition in the Amazon (change from HIST: -105 Mg

164   yr^{-1}; CI: -53 to -152 Mg yr^{-1}) and enhanced Hg^0 emissions from soils newly exposed to light

165   (+35 Mg yr^{-1} ; CI: 28–275 Mg yr^{-1}). For the Amazon policy scenarios, we have also

166   considered the impact that fire-mediated forest clearing[53,54] has on biomass burning emissions

167   of Hg, which are 15 Mg yr^{-1} (CI: 10–17 Mg yr^{-1}) larger in BAU than HIST. The BAU

168   scenario shows atmospheric Hg^0 concentrations increasing up to 0.3 ng m^{-3} within the

169   Amazon region (Fig. S12); this would be a detectable change in Hg^0, comparable to the 0.5 ng

170   m^{-3} decrease between 1995–2015 in North American Hg^0 observations[55]. In the GOV

171   scenario, deforestation is slowed by the conservation measures, leading to smaller

172   perturbations in the dry deposition flux from HIST (-47 Mg yr^{-1} ; CI: -25 to -68 Mg yr^{-1}) and

173   the soil emission flux (+16 Mg yr^{-1}; CI: 12–126 Mg yr^{-1}) (Fig. 2b). Globally, the weakened

174   rainforest sink of Hg yields higher deposition of Hg to oceans compared to the reference

175   simulation (BAU – HIST = +108 Mg yr^{-1}; GOV – HIST = +44 Mg yr^{-1}). Deforestation can be

176   exacerbated through climate feedbacks, which are not considered in these policy scenarios.

177   For example, BAU projects that 40% of the Amazon will be deforested by 2050[27], which

178   could trigger a tipping point with widespread transition of the rainforest to a savannah biome

179   under diminished regional moisture recycling[56]. To evaluate this, we also re-ran an upper

180   limit scenario from our previous work[23] where the entire rainforest is converted to savannah

181   (SAV). In this case, a strong decline in Hg^0 dry deposition (-359 Mg yr^{-1}; CI: -210 to -503 Mg

182   yr^{-1}) and increase in Hg^0 soil emissions (+89 Mg yr^{-1}; CI: 68 to 652 Mg yr^{-1}) drive enhanced

183   inputs of Hg to the ocean (343 Mg yr^{-1}) (Fig. 2b).

184   This change in the fate of atmospheric Hg (deposition to ocean instead of land) affects

185   both the spatial distribution and bioavailability of Hg pollution. When sequestered in soils, Hg

186   has an estimated residence time on the order of hundreds of years, whereas in the surface

187   ocean Hg is recycled to the atmosphere within months to years[7,11]. Deforestation thus

188   increases the mobility of Hg by transferring Hg from locally-sequestered reservoirs to the

189   global pool. Human health risks are driven by exposure to the more toxic form of the element,

190   MeHg, which is produced through methylation in the environment[2,57]. Deforestation shifts Hg

191   inputs from land to the ocean, where Hg can more readily be methylated and bioaccumulate to

192   dangerous levels in commercial fish. Methylation and bioaccumulation of Hg can also occur

193   in forested soils, but MeHg levels in aquatic ecosystems are generally much higher (overall

194   global ocean average = 15%)[58] than in Amazonian soils (1–5%)[33,59]. In addition, the long

195   length of aquatic food chains leads to high levels of MeHg in commonly consumed fish

196   species at higher trophic levels (e.g., tuna, cod, and swordfish)[57].
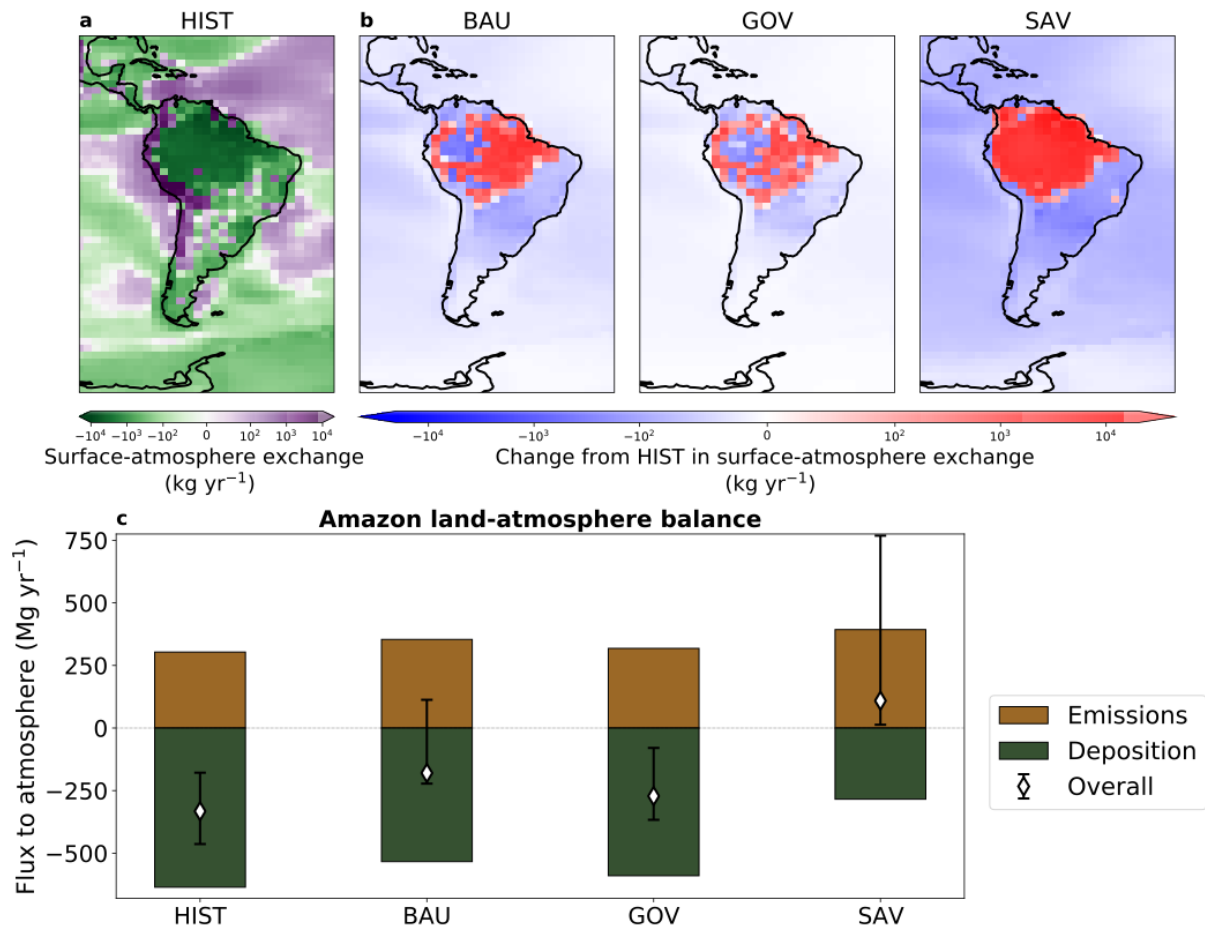
Figure 2. Impacts of Amazon deforestation scenarios on surface-atmosphere Hg exchange. a.
The simulated surface-atmosphere exchange (net deposition is negative and net emission is positive)
of Hg in the reference simulation (HIST). **b.** Changes in exchange fluxes from HIST are shown for the
deforestation scenarios: Business-as-usual (BAU), Governance (GOV), and Savannization (SAV);
negative values refer to increased net fluxes to the surface compared to HIST and positive values refer
to increased net fluxes to the atmosphere. **c.** Total simulated fluxes of Hg emissions and deposition are
calculated for the Amazon region in each scenario. White diamonds illustrate the net flux of Hg to the
atmosphere (= emissions – deposition) and error bars refer to the 95% confidence interval based on
model parameter uncertainties.

Deforestation policy substantially impacts the soil mass balance of Hg in the Amazon
region, illustrated by our modeling simulations (Fig. 2c) and available field observations (Fig.
S3). If agricultural expansion continues as in BAU, the Amazon sink of atmospheric Hg is
weakened by 153 Mg yr^{-1} (CI: 97–418 Mg yr^{-1}) (Fig. 2c). Under the more moderate GOV
scenario, the Amazon Hg sink (272 Mg yr^{-1}; CI: 79–367 Mg yr^{-1}) is better preserved, though
still 18% (CI: 14–65%) smaller than HIST. Stricter conservation policies in GOV yield an
additional 92 Mg yr^{-1} (CI: 59–234 Mg yr^{-1}) of Hg sequestered in the Amazon compared to
BAU. The SAV scenario illustrates that additional climate feedbacks could flip the Amazon
from a net Hg sink to a source (+109 Mg yr^{-1}; CI: 13–768 Mg yr^{-1}). These Hg projections
parallel recent findings on Amazon carbon cycling, which have demonstrated that climate

218 change and deforestation are turning the Amazon into a CO_2 source[25]. In addition to

219 atmosphere-terrestrial exchange fluxes, soil erosion of Hg can also be altered due to

220 deforestation. We applied a soil erosion model GloSEM[21,60] to evaluate the impact of

221 deforestation on erosion in the Amazon basin (Supplementary Information Section S6). In

222 terms of Hg flux magnitudes, perturbations to erosion are smaller (<15%) than changes to the

223 atmosphere-terrestrial exchange fluxes (Section S6), which is supported by field studies[48].

224 Nevertheless, deforestation also enhances Hg erosion in both scenarios (BAU: +33%; GOV:

225 +14%), accelerating the transfer of terrestrial Hg to aquatic ecosystems.

226

Quantifying the Hg mitigation potential of reforestation

228 Reforestation has been identified as a potential mitigation approach for climate change, by

229 strengthening the terrestrial CO_2 sink[31,61]. To investigate the concurrent strengthening of the

230 terrestrial Hg sink and the impacts on Hg cycling, we considered a global reforestation

231 scenario (RFR) based on the Global Reforestation Potential Map[31,62], which identified areas

232 suitable for reforestation worldwide (i.e., not including croplands or areas where forests are

233 not native). Figure 3 maps the impacts of reforestation on Hg surface-atmosphere exchange,

234 comparing to the reference HIST simulation. Globally, RFR enhances uptake of Hg on land

235 by 98 Mg yr^{-1} (CI: 64–449 Mg yr^{-1}), thereby reducing Hg deposition to oceans. Reforestation

236 could thus take up approximately 5% of the anthropogenic Hg emission flux (~2200 Mg

237 yr^{-1})[9]. In addition to the targeted benefits for biodiversity and climate change mitigation[31],

238 reforestation could moderately reduce levels of Hg in marine ecosystems, and thus

239 commercial fish. Nevertheless, the magnitude of reforestation impact (5% of primary

240 emissions) illustrates that reforestation is not a substitute for implementing extensive cuts to

241 primary Hg emissions, like in the CO_2 context[29].

242   Potential reforestation opportunities for Hg are dominated by the Amazon and

243 Atlantic forest regions in South America (71 Mg yr^{-1}, 72% of total land sink impact) (Fig. 3).

244 The potential reforestation impact in Northern extratropical areas alone on emissions (-29 Mg

245 yr^{-1}) cannot compensate for deforestation Hg emissions in the Amazon (BAU: +153 Mg yr^{-1};

246 GOV: +61 Mg yr^{-1}). Overall, more information would be needed to compare the potentials of

247 reforestation and conservation policies on a global scale, as the deforestation policy scenarios

248 focused only on a specific region (the Amazon); future research could study conservation

249 impacts in other tropical regions with high Hg deforestation emissions (Fig. 1) (e.g., in Africa

250 and Southeast Asia).

251
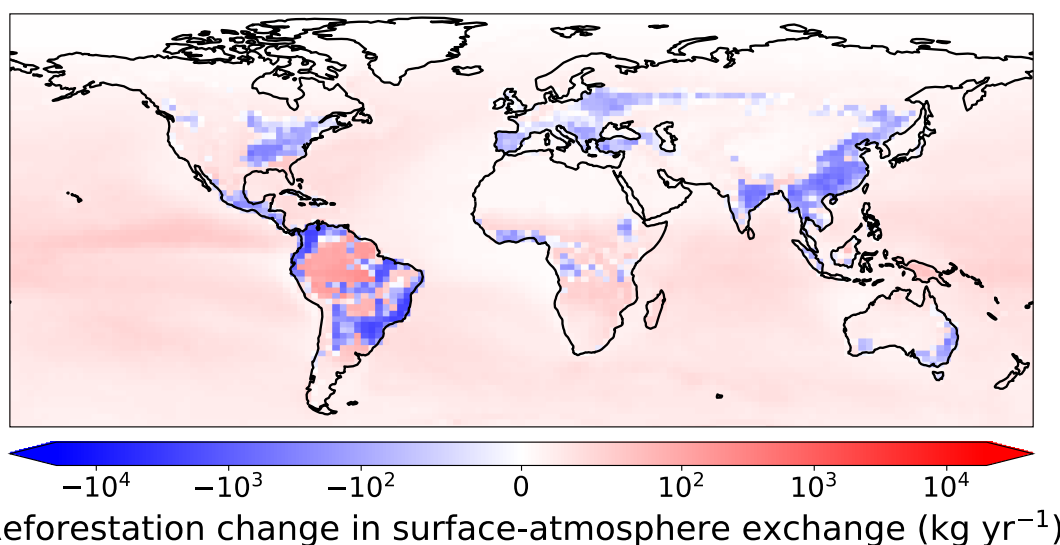
Figure 3. Enhanced land sink of Hg with reforestation. The impact of the potential reforestation
(RFR) scenario on surface-atmosphere exchange. The differences from the reference (HIST)
simulation are shown, with negative values referring to increased net fluxes to the surface and positive
values referring to increased net fluxes to the atmosphere.

257

Implications for global Hg policy and caveats

259 Land use policy has been largely unexplored as a lever to mitigate Hg pollution. On the global

260 scale, the estimated deforestation-driven Hg emissions in 2015 (217 Mg yr^{-1}; CI: 134–1650

261 Mg yr^{-1}) correspond to 10% of the global primary anthropogenic emissions[9] (2222 Mg yr^{-1})

262 (Fig. 4a). Therefore, though cutting primary anthropogenic emissions remains a priority,

263 deforestation fluxes should not be overlooked in assessments of Hg pollution, especially for

264 countries in the tropics (Fig. 1b). The potential of Amazon conservation and global

265 reforestation to reduce net Hg emissions in the future is substantial compared to previously

266 quantified policies aimed at tackling primary anthropogenic emissions (Fig. 4b). Potential

267 emissions reductions from Amazon conservation (92 Mg yr^{-1}) and global reforestation (98 Mg

268 yr^{-1}) are within the range of impacts of past policy and future policy scenarios aimed at

269 reducing Hg from specific anthropogenic sources or due to national climate and air pollution

270 policies (5–262 Mg yr^{-1}) (refs.[63–68]). Emissions reductions from land policies are different

271 from primary emissions reductions in that their efficacy depends on whether the storage of Hg

272 in soils is over a long-term period. Similar to CO_2, the potential benefits of enhanced Hg

273 uptake on land can be reversed by human or natural disturbances, e.g., by climate change

274 increasing the frequency of wildfires — which re-emit Hg and carbon from terrestrial

275   ecosystems — and droughts — which reduce Hg and CO_2 uptake by plants[31,69]. Thus,

276   mitigation of Hg pollution by conserving and increasing forest area can only be realized with

277   concurrent efforts to sustainably manage land areas and preventing severe climate change.

278   The potential of sustainable land use to mitigate Hg pollution could enable collaborations

279   between the Minamata Convention and other global policy efforts to reduce deforestation,

280   e.g., the 2021 Glasgow Declaration[70].

281
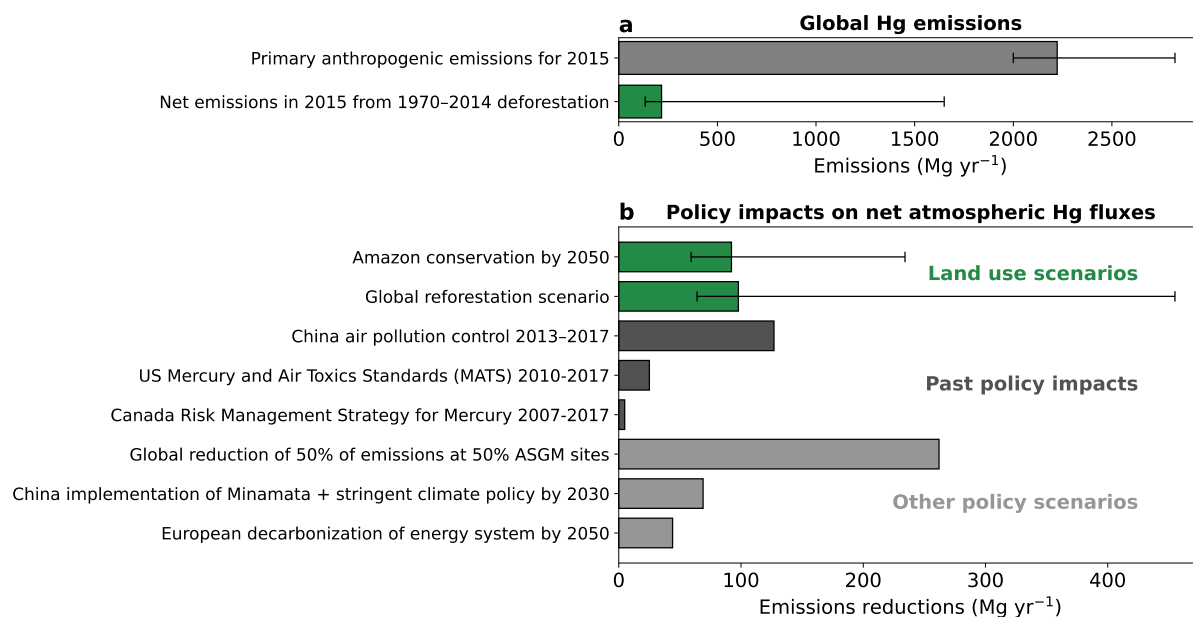
282

283   **Figure 4. Potential of land use policies to reduce net Hg fluxes to the atmosphere. a.** Comparing
284   global 2015 emissions from primary anthropogenic emissions[9,51] and deforestation-driven emissions,
285   assuming a 45-year time horizon (1970–2014 deforested areas). **b.** Net Hg emissions reductions from
286   land use policies are compared to primary anthropogenic emissions policies, whose impacts have been
287   quantified in the literature[63–68]. ASGM refers to artisanal and small-scale gold mining. For land use
288   scenarios, "Amazon conservation by 2050" refers to the net emissions reductions in the 2050
289   governance (GOV) from the business-as-usual (BAU) simulations and "Global reforestation scenario"
290   compares the net emissions reductions in the reforestation scenario (GOV) compared to the reference
291   simulation (HIST). Error bars refer to the 95% confidence interval based on model parameter
292   uncertainties.

293

294   The current work provides an initial assessment of the global emissions of Hg from

295   deforestation, which can spur future investigation into the impact of LULCC on Hg. Other

296   LULCC processes (e.g., wood harvest and agricultural practices) may also affect Hg fluxes

297   but have not been considered within this study. As well, due to the early stage of Hg research,

298   we do not yet have the same level of information for Hg that is commonly included in

299   LULCC assessments for carbon, including temporal information on the release of Hg from

300   soils and Hg uptake rates during regrowth of vegetation[22]. There is a lack of measurements in

301   relevant regions (e.g., Afrotropic and Indomalayan) to constrain the response of Hg fluxes to

302   deforestation, contributing uncertainty to this work. Further development of terrestrial Hg

303   cycles and LULCC processes within Earth system models[71] will be vital to investigate the

304   evolution of the Hg land sink over time and the effect on environmental Hg risks. Ultimately,

305   mitigation of global Hg pollution depends not only on reducing primary anthropogenic

306   emissions, but also reducing anthropogenic activities like deforestation that re-mobilize

307   legacy Hg.

308

309   ## Methods

310   **Atmospheric Hg model (GEOS-Chem) description**

311   In this study, we use GEOS-Chem v12.8.1 with Hg^0 dry deposition updates from Feinberg et

312   al.[23]. The global model is run at $2.0° \times 2.5°$ horizontal resolution and 47 vertical layers up to

313   80 km altitude. The model tracks emissions, transport, chemistry, and deposition of Hg in

314   three chemical tracers: elemental mercury (Hg^0), oxidized mercury (Hg^{II}), and particulate-

315   bound mercury (Hg^P). Atmospheric transport of Hg species is based on MERRA-2 reanalysis

316   meteorological data[72]. The Hg chemical mechanism assumes that Br is the primary Hg

317   oxidant and uses offline monthly maps of previously-calculated oxidant concentrations to

318   drive chemistry[73,74]. The aqueous photoreduction rate of Hg^{II} to Hg^0 is parametrized as

319   depending on the organic aerosol concentration and the NO_2 photolysis rate[73].

320   The wet removal of oxidized Hg (Hg^{II} and Hg^P) from the atmosphere is calculated in

321   online parametrizations considering large-scale and convective scavenging of gas and

322   particulate species[75,76]. Dry deposition in GEOS-Chem is calculated using a resistance-based

323   approach[77,78], which determines the dry deposition velocities depending on meteorology (e.g.,

324   temperature and windspeed), land surface parameters (e.g., land type and leaf area index,

325   LAI), and compound-specific parameters (biological reactivity, f_0, and solubility, H^*). For

326   Hg^0, f_0 is set to 0.2 within the Amazon rainforest and 3×10^{-5} elsewhere, which was found to

327   yield the best agreement with measurements of Hg^0 vegetation uptake[23]. The solubility of Hg^0

328   is low ($H^* = 0.11$ M atm^{-1})[79], whereas gaseous Hg^{II} is assumed to be highly soluble ($H^* =$

329   10^{14} M atm^{-1}) and biologically unreactive ($f_0 = 0$). Dry deposition of Hg^P is determined

330   according to the aerosol deposition parameterization in GEOS-Chem[80,81]. Dry deposition is

331   calculated separately over each land type within a grid cell (e.g., rainforest, grassland,

332   cropland, etc.) and then an overall area-weighted average is calculated for the grid cell.

333   GEOS-Chem accounts for 73 land types based on the Gibbs[82] land cover product. The LAI

334   data for this study is taken from a reprocessed version of the Moderate Resolution Imaging

335   Spectroradiometer (MODIS) satellite product[83]. Dry deposition of Hg^0 over the ocean is not

336 calculated within the resistance-based scheme, as it is instead accounted for in the air-sea

337 exchange parametrization[84].

338 Anthropogenic Hg emissions follow AMAP/UNEP estimates[51] for 2015. Biomass

339 burning emissions are taken from the Global Fire Emissions Database (GFED) v4.1s (ref.[85]).

340 Emissions of Hg^0 from snow and geogenic sources, as well as prompt recycling of 20% of

341 recently deposited oxidized mercury (Hg^{2+}) to land, follow Selin et al.[86]. We use fixed

342 concentrations of Hg^0 in the surface ocean based on the MITgcm 3-D ocean model[73] to

343 calculate the Hg^0 air-sea exchange[84]. We adopted a new formulation[87] for the soil Hg^0

344 emissions parametrization (Supplementary Information, Section S1):

345
$$E_{\text{soil}} = aC^b R_g^c \qquad (1)$$

346 where E_{soil} is the Hg^0 emissions from soil (units ng m^{-2} h^{-1}), C is the concentration of Hg in

347 soils, R_g is solar radiation flux at the ground, and a, b, and c, are coefficients (set to 71, 2.5,

348 and 0.76, respectively). We have tuned the coefficients of this parametrization to match

349 available soil emissions measurements from the Amazon and extratropics (Section S2). The

350 soil concentration map of Hg (C) was calculated using the method of Selin et al.[86], deriving

351 the spatial distribution of soil concentrations by first assuming a steady state balance between

352 land emissions and deposition in the preindustrial and subsequently increasing soil

353 concentrations according to the distribution of anthropogenic Hg deposition. As in Selin et

354 al.[86], the solar radiation at ground (R_g) is determined by considering attenuation of the solar

355 radiation flux (R_S) by shading from the overhead canopy, parametrized by the LAI:

356
$$R_g = R_S \exp\left(-\frac{\alpha \text{LAI}}{\cos\theta}\right) \qquad (2)$$

357 where $\alpha = 0.5$, assuming extinction from a random angular distribution of leaves[88] and θ is

358 the solar zenith angle. We have also updated GEOS-Chem to calculate soil emissions at the

359 sub-grid scale for each land use category contained within the grid cell.

360

361 **Reference (HIST) simulation**

362 We ran a GEOS-Chem simulation for the land cover and LAI conditions of the year 2003

363 (HIST simulation). The year 2003 is the earliest year where continuous reprocessed MODIS

364 LAI data is fully available[89] and is the baseline year in the Amazon deforestation policy

365 scenarios[27]. To highlight the role of land cover changes alone, we keep meteorological

366 conditions constant by running all simulations with meteorology for 2014–2015. We consider

367 the first year as spinup to equilibrate the new land cover conditions, and analyze simulation

368 differences for the meteorological year 2015.

369

370 **Estimating historical global deforestation-driven Hg emissions**

371 We calculate regional emissions factors (EFs) for deforestation through conducting

372 perturbation experiments in GEOS-Chem. We distinguish emission factors for the following

373 regions based on biogeographic realms[90] or specific Hg-relevant characteristics: Palearctic,

374 Nearctic, Afrotropic, Neotropic, Australasia & Oceania, Indomalaya, China, and the Amazon

375 rainforest (mapped in Fig. S6). We separate China into its own region as soil Hg

376 concentrations are higher than surrounding areas due to historical Hg emissions. The Amazon

377 rainforest is separated from other Neotropic forests due to it having higher observed

378 vegetation uptake fluxes and a different assigned f_0 parameter in the model dry deposition

379 scheme[23]. For each region, we conduct a simulation where we perturb the land cover in grid

380 cells that experience deforestation during 2000–2014 in the $0.25° \times 0.25°$ resolution CMIP6

381 Land-Use Harmonization (LUH2) dataset[49]. For these grid cells, we replace forest land cover

382 with the most common agricultural land cover relevant to the region: "Crops and Town"

383 (Afrotropic, Indomalaya, Palearctic, Australasia & Oceania, and China), "Corns and Beans

384 Croplands" (Neotropic and Nearctic), and "Fields and Woody Savannah" (Amazon). For the

385 new agricultural areas, the LAI is set to the average annual cycle for the existing agricultural

386 grid cells within the region. We run 8 deforestation (DFR) simulations (1 for each region)

387 over 2014–2015, comparing year 2015 fluxes to the HIST simulation. To calculate the net

388 emissions factor (EF) from deforestation, we calculate changes to the land-air exchange over

389 the deforested grid cells:

390
$$\text{EF} = \frac{(E_{\text{DFR}} - D_{\text{DFR}}) - (E_{\text{HIST}} - D_{\text{HIST}})}{A_{\text{DFR}}} \qquad (4)$$

391 where E refers to Hg emissions, D refers to Hg deposition, and A refers to the area that is

392 deforested in the simulation. The emissions factor represents the net emissions of Hg released

393 by a deforested area annually, in units Mg m^{-2} yr^{-1}. The assumption of linearity of the net

394 emissions to deforested area holds over simulations conducted in the Amazon with differing

395 spatial distributions of deforestation (Fig. S5), supporting an emissions factor approach to

396 deforestation. We compared calculated emissions factors with existing estimates from

397 observational and modeling studies[17,20,24,32–48], finding overlapping agreement for regions

398 where observational evidence is available (Fig. S4).

399   We apply the regional emissions factor to historical land use data from the LUH2

400 dataset to calculate emissions from deforestation. The LUH2 dataset was thoroughly

401 evaluated against Landsat satellite-based forest loss observations[91] for the 2000–2012 time

402 period[49]. We define gross deforested areas from the LUH2 dataset by summing the areas with

403 transitions from primary or secondary forest to a non-forest land type. This approach does not

404   consider LULCC fluxes due to harvesting of a forest without complete deforestation or the

405   regrowth of vegetation after clearing, due to a lack of corresponding observations for Hg to

406   constrain these parameters. Likewise, the emissions factors are assumed to be constant over

407   time, so a deforested area continues to have the same annual emissions over the considered

408   time horizon. In reality, deforested areas could have a recovery timescale as vegetation

409   regrows, which is accounted for in carbon LULCC fluxes[92]; for Hg, the response rate to

410   regrowth is largely unknown. To account for these uncertainties, we produce global and

411   country-level estimates of Hg emissions in 2015 due to deforestation by summing

412   deforestation over different time horizons: 15 years (2000–2014), 30 years (1985–2014), 45

413   years (1970–2014), and 60 years (1955–2014). We present the 45-year (1970–2014)

414   accumulated results in the main text, with the others presented in Fig. S7. The selected time

415   horizons represent a range of relevant time points to the potential recovery of deforested

416   areas, with previous carbon LULCC studies suggesting that forests recover their original

417   biomass within 75 years after deforestation[50].

418

419   **Future Amazon deforestation scenarios**

420   We employ deforestation scenarios from Soares-Filho et al.[27], who developed a model for

421   predicting the extent of deforestation within the Amazon based on environmental policies and

422   highway construction. They presented two scenarios for 2050, encompassing a range of future

423   deforestation trajectories: a Business as Usual (BAU) scenario and a Governance (GOV)

424   scenario. In the BAU scenario, recent deforestation trends continue into the future, assuming

425   that compliance with conservation laws remains low and no new areas will be protected. On

426   the other hand, the GOV scenario assumes the expansion of environmental legislation and

427   increased enforcement of protected areas will lead to a reduction in the deforestation rate.

428   Compared to the Amazon forest area in 2003 (5.3 million km^2), in 2050 the BAU scenario

429   projects 3.2 million km^2 remaining (-40% of 2003 area) and GOV projects 4.5 million km^2

430   remaining (-15%)[27]. We focus our analysis on comparing the forest coverage in the years

431   2003 and 2050, with these policy scenarios being the only available projections (to our

432   knowledge) forecasting likely ranges of deforestation for 2050 in the entire Amazon basin.

433   We translated these scenarios into required inputs for the calculations in GEOS-Chem

434   (spatially gridded land use categories, LAI, and biomass burning emissions). We used year

435   2003 data as the base maps for LAI and biomass burning datasets, with the HIST simulation

436   using these reference datasets. The Soares-Filho et al.[27] dataset assigns 1 km^2 pixels within

437   the Amazon basin as being forested, deforested, or agricultural areas for every year between

438 2003 and 2050. We regridded these annual datasets to $0.25° \times 0.25°$ resolution, the native

439 resolution of land use and LAI maps in GEOS-Chem. We calculated the relative change in

440 forested area in the scenarios for every $0.25° \times 0.25°$ grid cell. The rainforest land use

441 category in deforested grid cells is correspondingly reduced by this factor, with the lost land

442 area added to the land use category for "Fields and Woody Savanna". The LAI annual cycle

443 for existing Fields and Woody Savanna grid cells within the Amazon basin was spatially

444 averaged over 2003 and assigned to the deforested areas. Annual average LAI maps for the

445 Amazon scenarios used in GEOS-Chem are shown in Fig. S10. For these simulations, we

446 assume that conversion of forest to agricultural land within the Amazon is fire-mediated[53].

447 Gridded biomass burning emissions are calculated by multiplying the newly deforested areas

448 for each year by mean fire Hg emissions ($380\ \mu g\ m^{-2}\ yr^{-1}$) from two observational studies in

449 the Amazon[18,93]. An additional 50% of the emissions ($190\ \mu g\ m^{-2}\ yr^{-1}$) are released to the

450 atmosphere within the first year as post-burn Hg^0 emissions from soils[17]. To account for

451 seasonal differences in meteorology and realistic timing for forest clearing and burning[53], we

452 assumed that deforestation occurs at the start of June and deforestation biomass burning

453 emissions occur in August and September .

454   The BAU and GOV scenarios do not account for any land-climate feedbacks[27],

455 wherein deforestation of the rainforest can lead to reduced moisture recycling and widespread

456 *savannization* (conversion of rainforest to savanna)[56,94]. As an upper bound for this process,

457 we consider an extreme scenario (SAV) where the Amazon rainforest is fully converted to

458 savanna[95]. The impact of this scenario on Hg^0 deposition was previously quantified[23], but here

459 we reran the SAV simulation in GEOS-Chem to account for updates in the soil Hg^0 emissions

460 parametrization. In the analysis of results, we calculate fluxes for the Amazon region,

461 averaging over the area covered by the Soares-Filho et al.[27] deforestation projections (shown

462 in Fig. S9).

463

464 **Potential reforestation scenarios**

465 We apply a reforestation scenario (RFR) in GEOS-Chem based on the Global Reforestation

466 Potential map[31,62], which considers the binary potential of every $1\ km^2$ grid cell to be

467 converted from non-forest (<25% tree cover in 2000–2009) to forest (>25% tree cover). The

468 reforestation potential dataset does not include areas that are native non-forest land cover

469 types (e.g., grasslands) or cropland areas. We regridded the reforestation potential to $0.25° \times$

470 $0.25°$ resolution, calculating the area fraction suitable for reforestation at the model's input

471 grid resolution. For every grid cell where reforestation can occur, we identify the

472 corresponding biome in the Ecoregions2017 dataset[90] to determine the type of native forest

473 vegetation that would occur. If the corresponding biome of the grid cell is not a forest (e.g., in

474 cases where the coarse coastal grid cell of the model is assigned to water in the

475 Ecoregions2017 dataset), we identify the most common forest type in the 8 neighbouring grid

476 cells. The added forest is assumed to have a LAI annual cycle equal to the 2003 spatial

477 average for all grid cells in the corresponding biome and biogeographic realm (LAI_{biome}). For

478 grid cells that are not a forest land type in 2003, we subtract the reforested area fraction (f_{rfr})

479 from the original land type and add the reforested area fraction to the new forest land type.

480 We only reforest grid cells in the case where LAI_{biome} is larger than the original land type LAI

481 (LAI_{old}). Since the land map used in GEOS-Chem is at coarser resolution ($0.25° \times 0.25°$) than

482 the reforestation potential dataset ($1 \text{ km} \times 1 \text{ km}$), the reforested grid cell may already be a

483 forest land type in GEOS-Chem. In this case, we assume that the grid cell LAI (LAI_{new}) will

484 become denser due to the new reforested area:

$$LAI_{new} = LAI_{old} + f_{rfr} \cdot LAI_{biome} \quad (3)$$

486 The resultant average LAI map in the RFR scenario is shown in Fig. S11.

487

488 **Uncertainty analysis**

489 Due to the computational expense of conducting uncertainty analyses in the online GEOS-

490 Chem model, we employ offline Python-based models for Hg^0 dry deposition[96] and soil Hg^0

491 emissions to calculate uncertainties in the terrestrial-atmosphere Hg fluxes. The Hg^0 dry

492 deposition and soil emissions changes contribute the overwhelming majority (>98%) of the

493 response to deforestation. We consider the contributions of deposition parameters (f_0 in

494 different regions), soil emission parametrizations, the assumption for LAI for replaced land

495 types, and biomass burning emission factors (for the Amazon simulations) to the overall

496 uncertainty in fluxes. Uncertainty bounds of these parameters are tabulated in Table S4. We

497 sample 100 parameter combinations using Latin Hypercube sampling[97], a method which

498 samples the parameter space more efficiently than random sampling. The offline models were

499 run for the year 2015 using monthly average diurnal cycles ($12 \times 24 \text{ h} = 288$ timesteps) of

500 meteorological parameters, land surface parameters, and Hg^0 concentration fields. At this time

501 resolution, the offline models show sufficient accuracy to assess parameter uncertainties, with

502 maximum errors compared to online predictions of 1% for annual mean soil emissions and

503 5% for Hg^0 deposition. We conducted 100 simulations in the offline emissions and deposition

504 models for each studied scenario, calculating 95% confidence intervals from the 2.5[th] and

505   97.5th percentile values in the offline calculated fluxes. All uncertainty analysis Python scripts

506   are located in a Zenodo repository: (https://doi.org/10.5281/zenodo.7957157).

507

Acknowledgements

517

Author contributions

519   All authors conceived the study. M.J., J.B., and A.F. compiled Hg field data through literature

520   review. A.F. and P.B performed the simulations. All authors contributed to the data analysis.

521   A.F. wrote the draft of the paper with contributions and revisions from all authors.

522

Competing interests

524   The authors declare no competing interests.

525

Data availability

527   Simulation data supporting the results of this study are published in Zenodo

528   (https://doi.org/10.5281/zenodo.7957157) under a CC BY 4.0 license

529   (https://creativecommons.org/licenses/by/4.0/).

530

Code availability

532   Model and analysis codes involved in producing the results of this study are published in

533   Zenodo (https://doi.org/10.5281/zenodo.7957157).

534

References

536   1. Sheehan, M. C. *et al.* Global methylmercury exposure from seafood consumption and risk
537   of developmental neurotoxicity: a systematic review. *Bull. World Health Organ.* **92**, 254-
538   269F (2014).

2. Zhang, Y. *et al.* Global health effects of future atmospheric mercury emissions. *Nat Commun* **12**, 3035 (2021).

3. Bellanger, M. *et al.* Economic benefits of methylmercury exposure control in Europe: Monetary value of neurotoxicity prevention. *Environ Health* **12**, 3 (2013).

4. Outridge, P. M., Mason, R. P., Wang, F., Guerrero, S. & Heimbürger-Boavida, L. E. Updated Global and Oceanic Mercury Budgets for the United Nations Global Mercury Assessment 2018. *Environ. Sci. Technol.* acs.est.8b01246 (2018) doi:10.1021/acs.est.8b01246.

5. Shah, V. *et al.* Improved Mechanistic Model of the Atmospheric Redox Chemistry of Mercury. *Environ. Sci. Technol.* **55**, 14445–14456 (2021).

6. UNTC. *Minamata Convention on Mercury*. (2013).

7. Amos, H. M., Jacob, D. J., Streets, D. G. & Sunderland, E. M. Legacy impacts of all-time anthropogenic emissions on the global mercury cycle. *Global Biogeochem. Cycles* **27**, 410–421 (2013).

8. Zhou, J., Obrist, D., Dastoor, A., Jiskra, M. & Ryjkov, A. Vegetation uptake of mercury and impacts on global cycling. *Nat. Rev. Earth Environ.* **2**, 269–284 (2021).

9. UNEP. *Global Mercury Assessment 2018*. (UN Environment Programme, Chemicals and Health Branch. Geneva, Switzerland, 2019).

10. Schaefer, K. *et al.* Potential impacts of mercury released from thawing permafrost. *Nat Commun* **11**, 4650 (2020).

11. Smith-Downey, N. V., Sunderland, E. M. & Jacob, D. J. Anthropogenic impacts on global storage and emissions of mercury from terrestrial soils: Insights from a new global model. *J. Geophys. Res.* **115**, G03008 (2010).

12. Jiskra, M. *et al.* A vegetation control on seasonal variations in global atmospheric mercury concentrations. *Nature Geosci* **11**, 244–250 (2018).

13. Fostier, A. H., Melendez-Perez, J. J. & Richter, L. Litter mercury deposition in the Amazonian rainforest. *Environ. Pollut.* **206**, 605–610 (2015).

14. IPCC. *Climate Change and Land: an IPCC special report on climate change, desertification, land degradation, sustainable land management, food security, and greenhouse gas fluxes in terrestrial ecosystems*. (2019).

15. Zhang, H., Holmes, C. D. & Wu, S. Impacts of changes in climate, land use and land cover on atmospheric mercury. *Atmos. Environ.* **141**, 230–244 (2016).

16. UNFCC. *The Paris Agreement*. (2015).

17. Carpi, A., Fostier, A. H., Orta, O. R., dos Santos, J. C. & Gittings, M. Gaseous mercury emissions from soil following forest loss and land use changes: Field experiments in the United States and Brazil. *Atmos. Environ.* **96**, 423–429 (2014).

18. Melendez-Perez, J. J. *et al.* Soil and biomass mercury emissions during a prescribed fire in the Amazonian rain forest. *Atmospheric Environment* **96**, 415–422 (2014).

19. Roulet, M. *et al.* Effects of Recent Human Colonization on the Presence of Mercury in Amazonian Ecosystems. *Water Air Soil Pollut.* **112**, 297–313 (1999).

20. Fostier, A. H. *et al.* Mercury fluxes in a natural forested Amazonian catchment (Serra do Navio, Amapá State, Brazil). *Sci. Total Environ.* **260**, 201–211 (2000).

21. Borrelli, P. *et al.* Land use and climate change impacts on global soil erosion by water (2015-2070). *Proc. Natl. Acad. Sci. U.S.A.* **117**, 21994–22001 (2020).

22. Obermeier, W. A. *et al.* Modelled land use and land cover change emissions – a spatio-temporal comparison of different approaches. *Earth Syst. Dynam.* **12**, 635–670 (2021).

23. Feinberg, A., Dlamini, T., Jiskra, M., Shah, V. & Selin, N. E. Evaluating atmospheric mercury (Hg) uptake by vegetation in a chemistry-transport model. *Environ. Sci.: Processes Impacts* **24**, 1303–1318 (2022).

24. Wang, X. *et al.* Emission-dominated gas exchange of elemental mercury vapor over natural surfaces in China. *Atmos. Chem. Phys.* **16**, 11125–11143 (2016).

590   25. Gatti, L. V. *et al.* Amazonia as a carbon source linked to deforestation and climate
591   change. *Nature* **595**, 388–393 (2021).
592   26. Tyukavina, A. *et al.* Types and rates of forest disturbance in Brazilian Legal Amazon,
593   2000–2013. *Sci. Adv.* **3**, e1601047 (2017).
594   27. Soares-Filho, B. S. *et al.* Modelling conservation in the Amazon basin. *Nature* **440**, 520–
595   523 (2006).
596   28. IPCC. Summary for Policymakers. in *Climate Change 2022: Mitigation of Climate*
597   *Change. Contribution of Working Group III to the Sixth Assessment Report of the*
598   *Intergovernmental Panel on Climate Change* ([P.R. Shukla, J. Skea, R. Slade, A. Al
599   Khourdajie, R. van Diemen, D. McCollum, M. Pathak, S. Some, P. Vyas, R. Fradera, M.
600   Belkacemi, A. Hasija, G. Lisboa, S. Luz, J. Malley, (eds.)]. Cambridge University Press,
601   Cambridge, UK and New York, NY, USA).
602   29. Holl, K. D. & Brancalion, P. H. S. Tree planting is not a simple solution. *Science* **368**,
603   580–581 (2020).
604   30. Portmann, R. *et al.* Global forestation and deforestation affect remote climate via adjusted
605   atmosphere and ocean circulation. *Nat Commun* **13**, 5569 (2022).
606   31. Griscom, B. W. *et al.* Natural climate solutions. *Proc. Natl. Acad. Sci. U.S.A.* **114**, 11645–
607   11650 (2017).
608   32. Gamby, R. L., Hammerschmidt, C. R., Costello, D. M., Lamborg, C. H. & Runkle, J. R.
609   Deforestation and cultivation mobilize mercury from topsoil. *Science of The Total*
610   *Environment* **532**, 467–473 (2015).
611   33. Gerson, J. R. *et al.* Amazon forests capture high levels of atmospheric mercury pollution
612   from artisanal gold mining. *Nat Commun* **13**, 559 (2022).
613   34. Almeida, M. D., Lacerda, L. D., Bastos, W. R. & Herrmann, J. C. Mercury loss from soils
614   following conversion from forest to pasture in Rondônia, Western Amazon, Brazil.
615   *Environmental Pollution* **137**, 179–186 (2005).
616   35. Almeida, M. D., Marins, R. V., Paraquetti, H. H. M., Bastos, W. R. & Lacerda, L. D.
617   Mercury degassing from forested and open field soils in Rondônia, Western Amazon,
618   Brazil. *Chemosphere* **77**, 60–66 (2009).
619   36. Lacerda, L. D., de Souza, M. & Ribeiro, M. G. The effects of land use change on mercury
620   distribution in soils of Alta Floresta, Southern Amazon. *Environmental Pollution* **129**,
621   247–255 (2004).
622   37. Béliveau, A., Lucotte, M., Davidson, R., do Canto Lopes, L. O. & Paquet, S. Early Hg
623   mobility in cultivated tropical soils one year after slash-and-burn of the primary forest, in
624   the Brazilian Amazon. *Science of The Total Environment* **407**, 4480–4489 (2009).
625   38. Béliveau, A. *et al.* Reduction of soil erosion and mercury losses in agroforestry systems
626   compared to forests and cultivated fields in the Brazilian Amazon. *Journal of*
627   *Environmental Management* **203**, 522–532 (2017).
628   39. Patry, C., Davidson, R., Lucotte, M. & Béliveau, A. Impact of forested fallows on fertility
629   and mercury content in soils of the Tapajós River region, Brazilian Amazon. *Science of*
630   *The Total Environment* **458–460**, 228–237 (2013).
631   40. Comte, I. *et al.* Impacts of Land Uses on Mercury Retention in Long-Time Cultivated
632   Soils, Brazilian Amazon. *Water Air Soil Pollut* **224**, 1515 (2013).
633   41. Magarelli, G. & Fostier, A. Influence of deforestation on the mercury air/soil exchange in
634   the Negro River Basin, Amazon. *Atmos. Environ.* **39**, 7518–7528 (2005).
635   42. Mainville, N. *et al.* Decrease of soil fertility and release of mercury following
636   deforestation in the Andean Amazon, Napo River Valley, Ecuador. *Science of The Total*
637   *Environment* **368**, 88–98 (2006).
638   43. Roulet, M. *et al.* The geochemistry of mercury in central Amazonian soils developed on
639   the Alter-do-Chão formation of the lower Tapajós River Valley, Pará state, Brazil.
640   *Science of The Total Environment* **223**, 1–24 (1998).

44. Wasserman, J. C., Campos, R. C., Hacon, S. de S., Farias, R. A. & Caires, S. M. Mercury in soils and sediments from gold mining liabilities in Southern Amazonia. *Quím. Nova* **30**, (2007).

45. Homann, P. S., Darbyshire, R. L., Bormann, B. T. & Morrissette, B. A. Forest Structure Affects Soil Mercury Losses in the Presence and Absence of Wildfire. *Environ. Sci. Technol.* **49**, 12714–12722 (2015).

46. Mazur, M. *et al.* Gaseous mercury fluxes from forest soils in response to forest harvesting intensity: A field manipulation experiment. *Science of The Total Environment* **496**, 678–687 (2014).

47. Ma, M., Wang, D., Sun, R., Shen, Y. & Huang, L. Gaseous mercury emissions from subtropical forested and open field soils in a national nature reserve, southwest China. *Atmospheric Environment* **64**, 116–123 (2013).

48. Eckley, C. S., Eagles-Smith, C., Tate, M. T. & Krabbenhoft, D. P. Surface-air mercury fluxes and a watershed mass balance in forested and harvested catchments. *Environmental Pollution* **277**, 116869 (2021).

49. Hurtt, G. C. *et al.* Harmonization of global land use change and management for the period 850–2100 (LUH2) for CMIP6. *Geosci. Model Dev.* **13**, 5425–5464 (2020).

50. Ramankutty, N. *et al.* Challenges to estimating carbon emissions from tropical deforestation. *Global Change Biol* **13**, 51–66 (2007).

51. Steenhuisen, F. & Wilson, S. J. Development and application of an updated geospatial distribution model for gridding 2015 global mercury emissions. *Atmos. Environ.* **211**, 138–150 (2019).

52. Pacyna, J. M. *et al.* Current and future levels of mercury atmospheric pollution on a global scale. *Atmos. Chem. Phys.* **16**, 12495–12511 (2016).

53. Crespo-Lopez, M. E. *et al.* Mercury: What can we learn from the Amazon? *Environment International* **146**, 106223 (2021).

54. Fisher, J. A. *et al.* A synthesis of mercury research in the Southern Hemisphere, part 2: Anthropogenic perturbations. *Ambio* **52**, 918–937 (2023).

55. Zhang, Y. *et al.* Observed decrease in atmospheric mercury explained by global decline in anthropogenic emissions. *Proc. Natl. Acad. Sci. U.S.A.* **113**, 526–531 (2016).

56. Lovejoy, T. E. & Nobre, C. Amazon Tipping Point. *Sci. Adv.* **4**, eaat2340 (2018).

57. Schartup, A. T. *et al.* Climate change and overfishing increase neurotoxicant in marine predators. *Nature* **572**, 648–650 (2019).

58. Zhang, Y., Soerensen, A. L., Schartup, A. T. & Sunderland, E. M. A Global Model for Methylmercury Formation and Uptake at the Base of Marine Food Webs. *Global Biogeochem. Cycles* **34**, (2020).

59. Roulet, M., Guimarães, J.R.D, & Lucotte, M. Methylmercury production and accumulation in sediments and soils of an amazonian floodplain – effect of seasonal inundation. *Water, Air, and Soil Pollution* **128**, 41–60 (2001).

60. Borrelli, P. *et al.* An assessment of the global impact of 21st century land use change on soil erosion. *Nat Commun* **8**, 2013 (2017).

61. Bastin, J.-F. *et al.* The global tree restoration potential. *Science* **365**, 76–79 (2019).

62. Griscom, B. W. *et al. Global Reforestation Potential Map.* https://doi.org/10.5281/zenodo.883444 (2017).

63. Liu, K. *et al.* Measure-Specific Effectiveness of Air Pollution Control on China's Atmospheric Mercury Concentration and Deposition during 2013–2017. *Environ. Sci. Technol.* **53**, 8938–8946 (2019).

64. EPA. *National Emission Standards for Hazardous Air Pollutants: Coal- and Oil-Fired Electric Utility Steam Generating Units—Reconsideration of Supplemental Finding and Residual Risk and Technology Review.* 2670–2704 https://www.govinfo.gov/content/pkg/FR-2019-02-07/pdf/2019-00936.pdf (2019).

65. Environment and Climate Change Canada. *Evaluation of the effectiveness of risk management measures for mercury*. 1–43 https://www.canada.ca/en/environment-climate-change/services/management-toxic-substances/evaluation-effectiveness-risk-management-measures-mercury.html (2020).

66. Bruno, D. E. *et al.* Reducing Mercury Emission Uncertainty from Artisanal and Small-Scale Gold Mining Using Bootstrap Confidence Intervals: An Assessment of Emission Reduction Scenarios. *Atmosphere* **14**, 62 (2022).

67. Mulvaney, K. M. *et al.* Mercury Benefits of Climate Policy in China: Addressing the Paris Agreement and the Minamata Convention Simultaneously. *Environ. Sci. Technol.* **54**, 1326–1335 (2020).

68. Rafaj, P., Cofala, J., Kuenen, J., Wyrwa, A. & Zyśk, J. Benefits of European Climate Policies for Mercury Air Pollution. *Atmosphere* **5**, 45–59 (2014).

69. Wohlgemuth, L. *et al.* Physiological and climate controls on foliar mercury uptake by European tree species. *Biogeosciences* **19**, 1335–1353 (2022).

70. COP26. *Glasgow Leaders' Declaration on Forests and Land Use*. https://ukcop26.org/glasgow-leaders-declaration-on-forests-and-land-use/ (2021).

71. Yuan, T. *et al.* Buffering effect of global vegetation on the air-land exchange of mercury: Insights from a novel terrestrial mercury model based on CESM2-CLM5. *Environment International* **174**, 107904 (2023).

72. Gelaro, R. *et al.* The Modern-Era Retrospective Analysis for Research and Applications, Version 2 (MERRA-2). *J. Clim.* **30**, 5419–5454 (2017).

73. Horowitz, H. M. *et al.* A new mechanism for atmospheric mercury redox chemistry: implications for the global mercury budget. *Atmos. Chem. Phys.* **17**, 6353–6371 (2017).

74. Schmidt, J. A. *et al.* Modeling the observed tropospheric BrO background: Importance of multiphase chemistry and implications for ozone, OH, and mercury. *J. Geophys. Res. Atmos.* **121**, 11,819-11,835 (2016).

75. Amos, H. M. *et al.* Gas-particle partitioning of atmospheric Hg(II) and its effect on global mercury deposition. *Atmos. Chem. Phys.* **12**, 591–603 (2012).

76. Liu, H., Jacob, D. J., Bey, I. & Yantosca, R. M. Constraints from ^{210}Pb and ^{7}Be on wet deposition and transport in a global three-dimensional chemical tracer model driven by assimilated meteorological fields. *J. Geophys. Res.* **106**, 12109–12128 (2001).

77. Wesely, M. L. Parameterization of surface resistances to gaseous dry deposition in regional-scale numerical models. *Atmos. Environ.* **23**, 1293–1304 (1989).

78. Wang, Y., Jacob, D. J. & Logan, J. A. Global simulation of tropospheric O$_3$-NO$_x$-hydrocarbon chemistry: 1. Model formulation. *J. Geophys. Res.* **103**, 10713–10725 (1998).

79. Lin, C.-J. & Pehkonen, S. O. The chemistry of atmospheric mercury: a review. *Atmos. Environ.* **33**, 2067–2079 (1999).

80. Fisher, J. A. *et al.* Sources, distribution, and acidity of sulfate–ammonium aerosol in the Arctic in winter–spring. *Atmos. Environ.* **45**, 7301–7318 (2011).

81. Zhang, L., Gong, S., Padro, J. & Barrie, L. A size-segregated particle dry deposition scheme for an atmospheric aerosol module. *Atmos. Environ.* **35**, 549–560 (2001).

82. Gibbs, H. K. Olson's Major World Ecosystem Complexes Ranked by Carbon in Live Vegetation: An Updated Database Using the GLC2000 Land Cover Product (NDP-017b). https://www.osti.gov/biblio/1389498, 2006. (2006).

83. Yuan, H., Dai, Y., Xiao, Z., Ji, D. & Shangguan, W. Reprocessing the MODIS Leaf Area Index products for land surface and climate modelling. *Remote Sens. Environ.* **115**, 1171–1187 (2011).

84. Strode, S. A. *et al.* Air-sea exchange in the global mercury cycle. *Global Biogeochem. Cycles* **21**, GB1017 (2007).

85. van der Werf, G. R. *et al.* Global fire emissions estimates during 1997–2016. *Earth Syst. Sci. Data* **9**, 697–720 (2017).

86. Selin, N. E. *et al.* Global 3-D land-ocean-atmosphere model for mercury: Present-day versus preindustrial cycles and anthropogenic enrichment factors for deposition. *Global Biogeochem. Cycles* **22**, GB2011 (2008).

87. Khan, T. R., Obrist, D., Agnan, Y., Selin, N. E. & Perlinger, J. A. Atmosphere-terrestrial exchange of gaseous elemental mercury: parameterization improvement through direct comparison with measured ecosystem fluxes. *Environ. Sci.: Processes Impacts* **21**, 1699–1712 (2019).

88. Verstraete, M. M. Radiation transfer in plant canopies: Transmission of direct solar radiation and the role of leaf orientation. *J. Geophys. Res.* **92**, 10985 (1987).

89. Lin, W. *et al.* Reprocessed MODIS Version 6.1 Leaf Area Index Dataset and Its Evaluation for Land Surface and Climate Modeling. *Remote Sensing* **15**, 1780 (2023).

90. Dinerstein, E. *et al.* An Ecoregion-Based Approach to Protecting Half the Terrestrial Realm. *BioScience* **67**, 534–545 (2017).

91. Hansen, M. C. *et al.* High-Resolution Global Maps of 21st-Century Forest Cover Change. *Science* **342**, 850–853 (2013).

92. Gasser, T. *et al.* Historical CO2 emissions from land use and land cover change and their uncertainty. *Biogeosciences* **17**, 4075–4101 (2020).

93. Michelazzo, P. A. M., Fostier, A. H., Magarelli, G., Santos, J. C. & de Carvalho, J. A. Mercury emissions from forest burning in southern Amazon. *Geophys. Res. Lett.* **37**, L09809 (2010).

94. Nobre, C. A. *et al.* Land-use and climate change risks in the Amazon and the need of a novel sustainable development paradigm. *Proc. Natl. Acad. Sci. U.S.A.* **113**, 10759–10768 (2016).

95. Alves de Oliveira, B. F., Bottino, M. J., Nobre, P. & Nobre, C. A. Deforestation and climate change are projected to increase heat stress risk in the Brazilian Amazon. *Commun. Earth Environ.* **2**, 207 (2021).

96. Feinberg, A. Offline dry deposition model from GEOS-Chem v1.0. (2022) doi:10.5281/zenodo.6498126.

97. McKay, M. D., Beckman, R. J. & Conover, W. J. Comparison of Three Methods for Selecting Values of Input Variables in the Analysis of Output from a Computer Code. *Technometrics* **21**, 239–245 (1979).

1

Supplementary Information (SI):

Deforestation as an anthropogenic driver of mercury pollution

4

Authors

Aryeh Feinberg[a], Martin Jiskra[b], Pasquale Borrelli[c], Jagannath Biswakarma[b,d], and Noelle E. Selin[a,e]

[a] *Institute for Data, Systems, and Society, Massachusetts Institute of Technology, Cambridge, MA, USA*

[b] *Environmental Geosciences, University of Basel, Basel, Switzerland*

[c] *Department of Science, Roma Tre University, Rome, Italy*

[d] *Department of Water Resources and Drinking Water, Eawag, Dübendorf, Switzerland*

[e] *Department of Earth, Atmospheric, and Planetary Sciences, Massachusetts Institute of Technology, Cambridge, MA, USA*

Correspondence to: arifeinberg@gmail.com (A.F.); martin.jiskra@gmail.com (M.J.)

Section S1. Soil emissions parameterization

19

20   We improved the model's parametrization of Hg^0 soil emissions by adopting a new

21   formulation for the parametrization, suggested by Khan et al.[1]:

$$E_{\text{soil}} = aC^b R_g^c \qquad \text{(S1)}$$

22

23   where E_{soil} are soil emissions (ng m^{-2} h^{-1}), C is the concentration of Hg in soils (ng g^{-1}) , R_g is

24   the solar radiation flux at the ground (W m^{-2}), and a, b, and c are coefficients.

25   As in Selin et al.[2], the solar radiation at ground (R_g) is determined by considering

26   attenuation of the solar radiation flux (R_S) by shading from the overhead canopy, parametrized

27   by the leaf area index (LAI):

$$R_g = R_S \exp\left(-\frac{\alpha \text{LAI}}{\cos\theta}\right) \qquad \text{(S2)}$$

28

29   where $\alpha = 0.5$, assuming extinction from a random angular distribution of leaves[3] and θ is the

30   solar zenith angle.

31   We compiled several relevant observational constraints for the parametrization in

32   Tables S1 and S2. Observational studies from the Amazon region (where most of the prior

33   field research has been concentrated) suggest that deforestation has a large impact on soil

34   emissions due to removal of canopy shading, showing factors of 1.8×, 6.7×, and >31× more

35   emissions in forested compared to deforested land plots (Table S1). Observational studies

36   from other regions find a similarly high sensitivity of soil emissions to the presence of forest:

37   open fields in China showed 6–10 times higher Hg emissions than forests[4] and logging in the

38   US flipped the surface-air Hg^0 flux from net deposition to net emissions (–2.2 µg m^{-2} yr^{-1} to

39   +5.5 µg m^{-2} yr^{-1}) (ref.[5]). For extratropical grassland soil emissions, we use the compiled

40   median values from Zhu et al.[6] and Agnan et al.[7]

41   We conducted a parameter sweep of a, b, and c, calculating globally-gridded soil

42   emissions using annual solar radiation data (Fig. S1). Sensitivity simulations showed that the

43   ratio of deforested to forested soil emissions in the Amazon (median value 6.7) can tune the

44   exponent for the radiation term (c in Eq. S1), i.e., the response of emissions to canopy

45   shading. The exponent for the soil concentration term (b) was tuned with the ratio of

46   deforested Amazon soil emissions (Table S1) to extratropical grassland soil emissions from

47   the Northern Hemisphere from two review studies[6,7] (overall Amazon to extratropical ratio of

48   5.3). Lastly, after these coefficients are tuned, the prefactor a is adjusted so that predicted

49   annual mean emissions match the observed median magnitudes of Amazon deforested soil

50   emissions (23 µg m^{-2} yr^{-1}) and extratropical grassland emissions (4.3 µg m^{-2} yr^{-1}).

51   We recognize the uncertainties in the observed data used to tune this parametrization,

52   and thus we constructed 100 alternative parametrizations that fit within observed data bounds

53 (Table S5). These parametrizations were applied in offline uncertainty analyses to assess 95%

54 confidence intervals in the fluxes driven by deforestation (Section S4).

55

56 **Table S1**. Literature review of available Hg^0 soil emission flux measurements from the Amazon
57 region, differentiated by land cover type.

Reference	Location	Site	Deforested Hg^0 flux ($\mu g \ m^{-2} \ yr^{-1}$)	Forested Hg^0 flux ($\mu g \ m^{-2} \ yr^{-1}$)	Flux ratio (deforest:forest)
Magarelli and Fostier[8]	Negro River Basin, Brazil	(1)	27 ± 9	0.6 ± 1.5	
		(2)	19	–1.0 ± 0.8	
		(3)	9.8 ± 0.7		
		Mean	18	–0.2	> 31[a]
Almeida et al.[9]	Rondônia, Brazil	(1)	79 ± 110	44 ± 18	1.8
Carpi et al.[10]	Acre, Brazil	(1)	19 ± 2	2.9 ± 0.8	6.7
		(2)	230[b]		
	Median		**23**	**1.8**	**6.7**

58 [a]upper limit calculated assuming the forested flux is equal to site (1), as site (2) shows negative overall flux

59 [b]this site was 2-months post-fire and soil temperatures were high; this flux is excluded from ratio calculations

60

61 **Table S2**. Observational constraints used to tune the soil emissions parametrization.

Constraint	Value	Reference	Coefficient constrained
Amazon deforested soil emissions ($\mu g \ m^{-2} \ yr^{-1}$)	23	Table S1	a
Extratropical grassland soil emissions ($\mu g \ m^{-2} \ yr^{-1}$)	4.3[†]	Zhu et al.[6]; Agnan et al.[7]	a
Ratio of Amazon to extratropical soil emissions	5.3	(23:4.3)	b
Ratio of deforested to forested Amazon soil emissions	6.7	Table S1	c

62 [†]average of grassland median Hg^0 fluxes from the two independent review studies
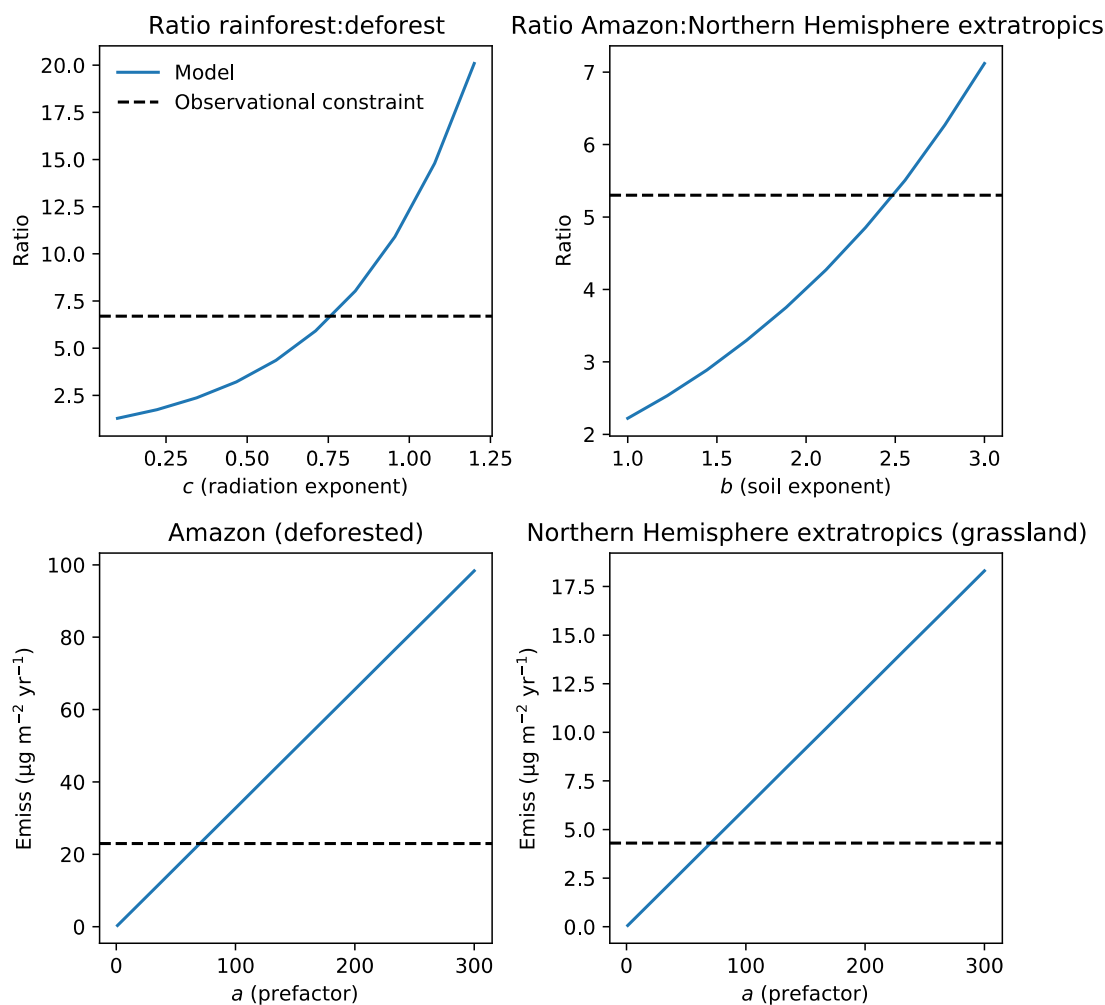
63

64 **Figure S1.** Parameter tuning (Eq. S1) to match observational constraints from Table S2.

65

66 The tuning procedure is illustrated in Fig. S1, yielding best matches for $a = 71$, $b = 2.5$, and

67 $c = 0.76$. We compare the gridded annual mean soil emissions from the previous soil emission

68 parametrization (GEOS-Chem v12.8) and the current study (Eq. S1) in Fig. S4. Global annual

69 mean soil Hg^0 emissions in the new parametrizations (954 Mg yr^{-1}) is similar to the

70 predictions from two GEOS-Chem studies[11,12] using the previous parametrization: 860 ± 440

71 Mg yr^{-1} and 910 Mg yr^{-1}. The spatial distribution of emissions (Fig. S2) shows a decrease in

72 vegetated regions (e.g., the Amazon and Congo rainforests) and an increase in regions with

73 high soil Hg concentrations (e.g., eastern China).

74
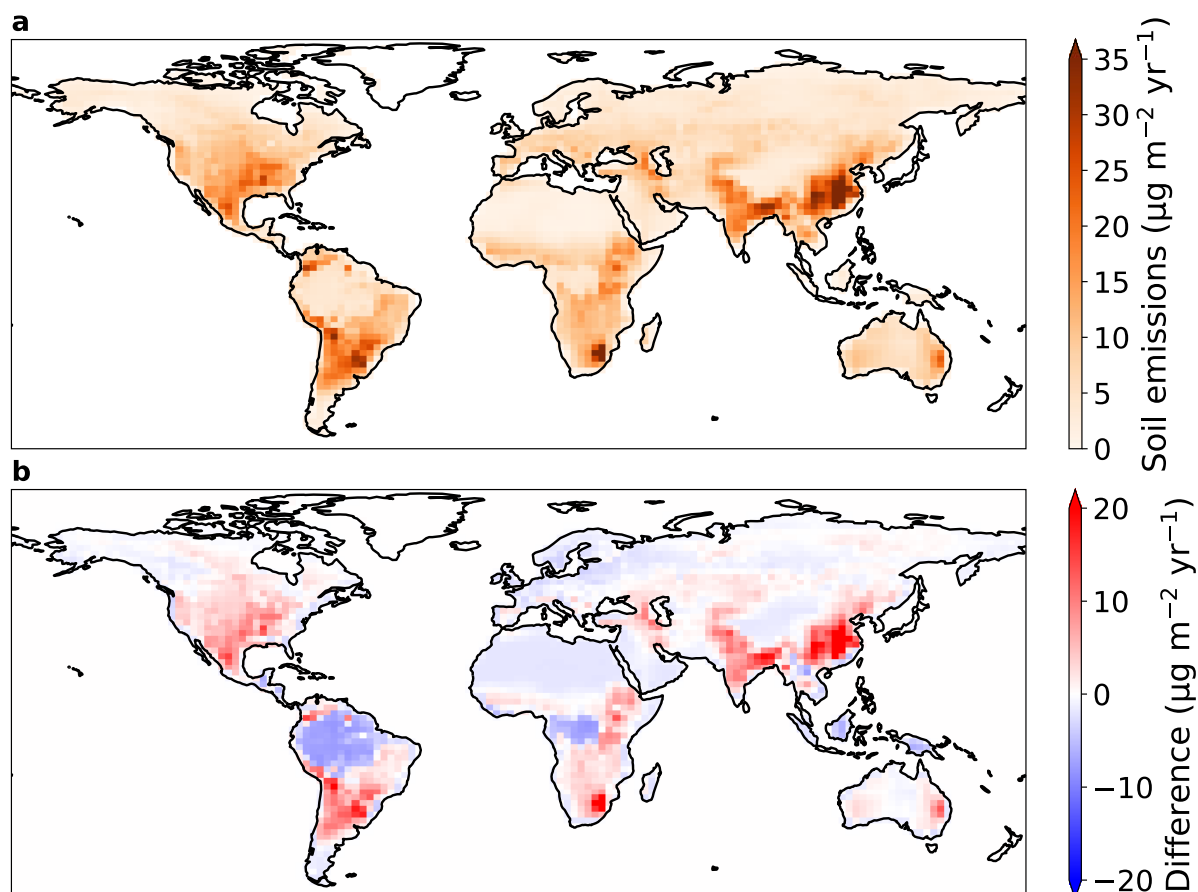
Figure S2. a. Annual mean soil emissions of Hg^0 with the new parametrization. **b.** Difference between new and old (GEOS-Chem v12.8) soil emissions parametrizations (new minus old).

Section S2. Observational constraints on deforestation Hg fluxes

There are several available sources of information that can be used to validate the deforestation emission factors (EF) calculated by GEOS-Chem (Fig. S4, SI Spreadsheet):

1) *Soil Hg concentration measurements of paired forest-deforested sites*:
Several studies, mainly focused in the Amazon rainforest, have measured the concentrations of Hg soils at deforested sites (C_d) and nearby forest (C_f) plots. For this analysis, we assume that the difference in these soil concentrations is due to mainly the change in atmospheric exchange, which is supported by the magnitude of modeled erosion fluxes (Section S6) and available measurements[5]. We use the following equation to convert the difference in these concentrations to a deforestation emission factor of Hg in Mg m^{-2} yr^{-1}:

$$\text{Total EF} = \frac{(C_d - C_f) \times \rho \times h}{t_d} \qquad \text{(S3)}$$

where ρ is the density of the soil, h is the depth of the soil layer, and t_d is the time since deforestation. In the US (Nearctic), there have been studies in Ohio[13] and Oregon[14] with

93   measurements of Hg in deforested and forested soils, which we use to calculate deforestation

94   EFs for the Nearctic. For the Amazon, more measurements are available (24 pairs of soil

95   plots) (refs.[8–10,15–25]). We compiled a literature database of studies that compared Hg

96   concentrations in deforested Amazonian soils with nearby forest plots (Fig. S3; SI

97   Spreadsheet). Deforested sites show a consistent decrease compared to paired forested sites

98   (p-value < 0.001; Wilcoxon signed-rank test), with the median decrease being 25 ng g^{-1} (10th–

99   90th percentile: 2–58 ng g^{-1}). To calculate a deforestation EF for the Amazon, we apply this

100   concentration decrease in Eq. S3 and assume an average Amazon soil density of 1.25 ng g^{-1}, a

101   surface soil layer of 10 cm, and that deforested soils in the literature studies were measured 10

102   years after deforestation.
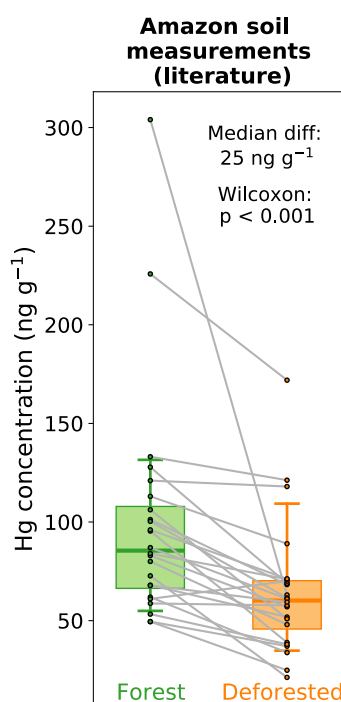
103

104   **Figure S3.** Measured Hg concentrations in forest (green) and deforested (orange) soils (0–20 cm

105   depth) from the literature ($n = 24$; refs.[8–10,15–25]). Box plots show the median values (solid lines),

106   interquartile range (shaded), and 10th and 90th percentiles (whiskers). Gray lines connect paired sites

107   from the same study. Listed p-value (<0.001) refers to the Wilcoxon signed-rank test of the null

108   hypothesis that paired forest and deforested sites come from the same distribution.

109

110   2) *Terrestrial-atmosphere exchange models validated by Hg observations*:

111   An estimate for the deforestation EF over China is available from the Wang et al.[26] modeling

112   study. We use their area-averaged mean fluxes over forest and agricultural land cover to

113   calculate a deforestation emission factor:

114              $$\text{Total EF} = (E_d - D_d) - (E_f - D_f) \qquad \text{(S4)}$$

115   where E_d and E_f are the natural emission fluxes (Mg m^{-2} yr^{-1}) from Chinese agricultural land

116   and forest, and D_d and D_f are the deposition fluxes (Mg m^{-2} yr^{-1}) to Chinese agricultural land

117   and forest. Although this EF estimate is model-based, the Wang et al.[26] model was validated

118   extensively with available terrestrial-atmosphere exchange measurements from China.

119

120   3) *Dynamic flux chamber measurements of forested and deforested soils*:

121   Additional studies investigating the impact of deforestation on atmospheric fluxes quantified

122   the response of soil emissions using dynamic flux chamber measurements[5,8–10,27,28]. We

123   compare these measurements to the soil-only EF modeled by GEOS-Chem. The soil emission

124   factors measured by the studies is calculated as the difference between soil emissions (Mg m^{-2}

125   yr^{-1}) over deforested and forested soils:

126      $$\text{Soil EF} = E_d - E_f \qquad \text{(S5)}$$

127

128   The comparison between GEOS-Chem simulated deforestation EFs and observation-

129   derived values is summarized in Fig. S4. Observations are only available from three regions

130   (Amazon, China and Nearctic). We found further references investigating the impact of

131   deforestation on Hg for the Palearctic region[29,30], yet these focused on measuring Hg

132   concentrations in aquatic media and methylation potential rather than soil concentrations or

133   atmospheric exchange. The modeled EF estimates and their uncertainties overlap with

134   observation-derived EFs for all 3 regions. If anything, the modeled best estimate used in

135   online simulations is conservative compared to available observations, showing generally

136   lower EFs (Fig. S4). However, it is unclear whether the sparse observations available are

137   representative of the overall region. The modeled EF uncertainty estimates cover 1-2 orders of

138   magnitude, emphasizing the current uncertainties in the response of Hg fluxes to

139   deforestation. The modeled error ranges appear well-calibrated in that they cover a similar

140   range as the variability in observation-derived fluxes. Figure S4 also reveals the regions

141   where no observations of the impact of deforestation on Hg cycling are currently available.

142   Specifically, the Afrotropic and Indomalayan domains would be priorities for future

143   measurement campaigns, given the current impact of deforestation in those regions (Fig. 1). It

144   remains unknown whether Southeast Asian and African rainforests show similarly high levels

145   of Hg in litterfall as the Amazon rainforest[31].
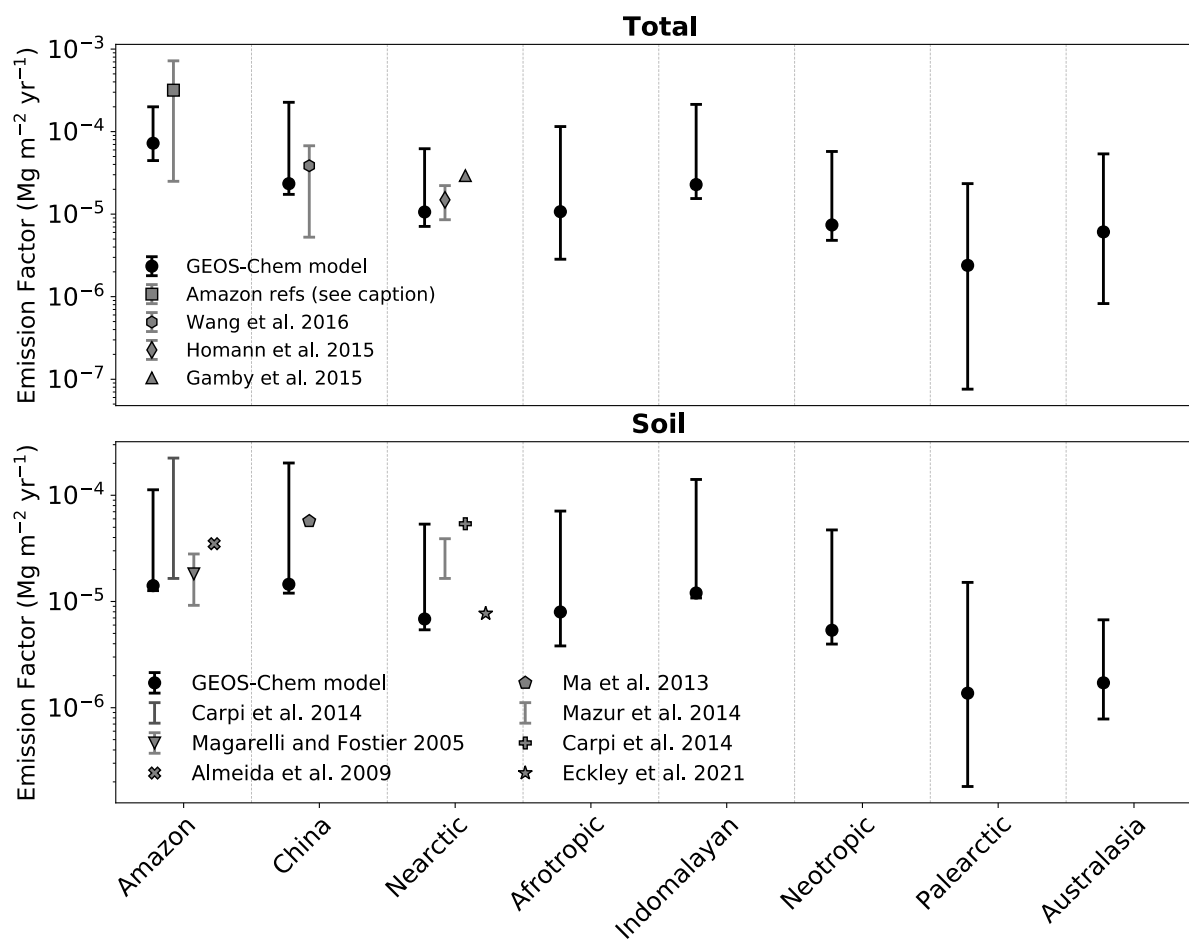
Figure S4. Comparison between modeled and observation-derived net emission factors (EFs) for deforestation in different regions. The upper panel shows total EFs and the lower panel shows the soil Hg^0 emissions component of deforestation EFs. Modeled circles show the best estimate (online simulations), while error bars show the 95% confidence interval due to model parameter uncertainties (calculated in offline simulations, Section S4). Observation estimates are from refs.[5,8–10,13–28], with the Amazon Total EF estimate based on measurements in Fig. S3. Observed error bars refer to uncertainty ranges when multiple plots were measured within a study (see SI spreadsheet for full calculations).

Section S3. Global deforestation-driven emissions estimates

We use perturbation simulations in which a set area within a region is deforested to calculate each deforestation EF. Using the Amazon deforestation scenario experiments, we explored the validity of our assumption to linearly relate the deforested area to the change in land-air fluxes (Fig. S5). In these four simulations — the reference simulation with 2003 forest cover (HIST), governance scenario for 2050 (GOV), business-as-usual for 2050 (BAU), and savannization (SAV) — different areas (both in spatial pattern and extent) were deforested in the Amazon region. The total fluxes from the Amazon basin for Hg^0 dry deposition, soil Hg^0 emissions, and the overall land-air balance of Hg all respond linearly ($R^2>0.98$) to the magnitude of the deforested area. Therefore, the approach of calculating deforestation EFs

165 and scaling these with deforested areas would likely not be highly sensitive to the spatial

166 distribution and amount of deforestation.
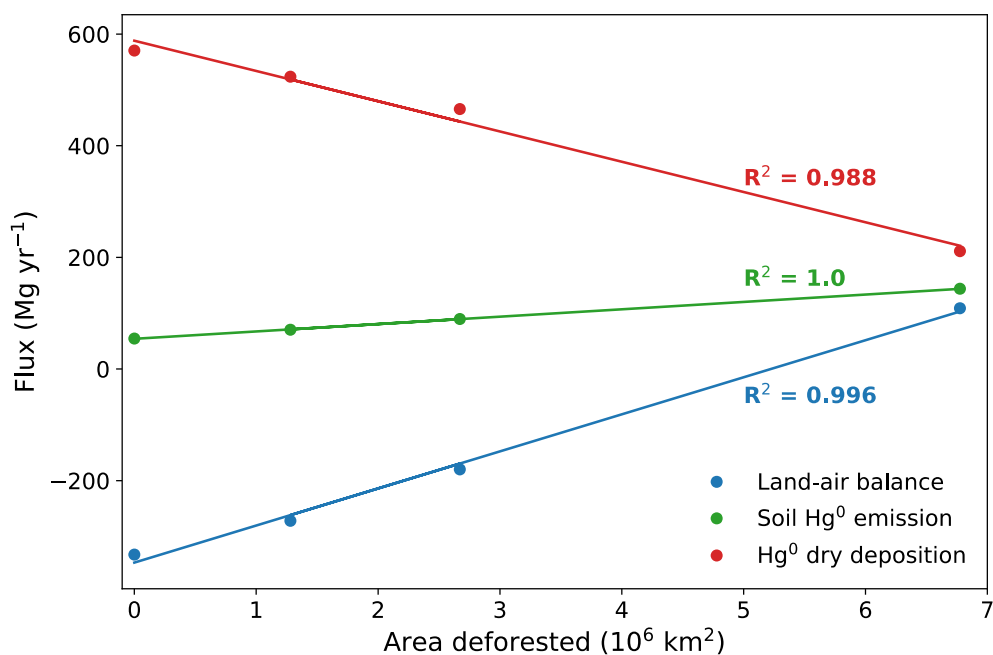
167

168 **Figure S5**. Relationship between land-air fluxes and the area deforested in GEOS-Chem simulations

169 for the Amazon rainforest. Fluxes are averaged over the Amazon rainforest domain and listed R^2

170 values refer to linear models.

171

172   Additional data related to the calculation of historical deforestation-driven emissions

173 of Hg are presented in this section. The maps defining the regions used in this study is shown

174 in Fig. S6. Table S3 tabulates the results from the perturbation simulations for the different

175 regions and the resultant emission factors. Fig. S7 explores the impact of choosing different

176 time horizons for the deforestation area on the calculated Hg emissions globally and by

177 country. Fig. S8 shows the map of Hg deforestation-driven emissions, assuming a 45 year

178 time horizon (deforestation area of 1970–2014 from the LUH2 dataset[32]).
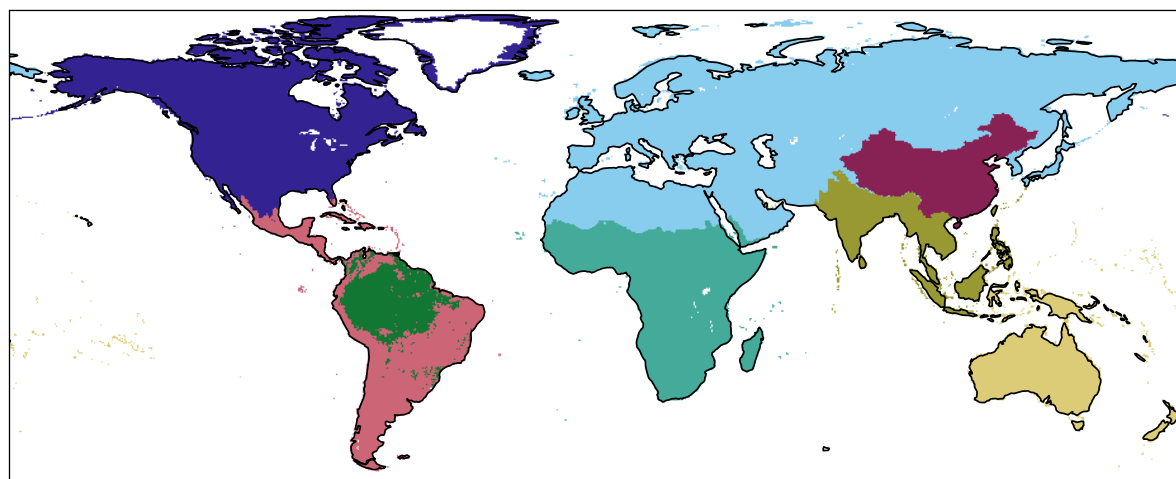
Palearctic   Nearctic   China   Australasia & Oceania

Afrotropic   Indomalaya   Amazon   Neotropic

Figure S6. Definition of regions used to calculate the deforestation emission factors.

**Table S3**. Results from the deforestation perturbation simulations in GEOS-Chem for determining the response of land-air fluxes to deforesting a specified area. Emissions factors are listed with the 95% confidence interval calculated in offline simulations assessing the uncertainties due to model parameters (Section S4).

| Realm	Area deforested (km^2)	Change in emissions (Mg yr^{-1})	Change in deposition (Mg yr^{-1})	Change in net emissions (Mg yr^{-1})	Emissions factor (Mg m^{-2} yr^{-1}) [95% confidence interval]
Afrotropic	3 644 969	29.1	-10.0	39.1	1.1×10^{-5} [2.8×10^{-6} to 1.2×10^{-4}]
Neotropic	2 422 577	13.0	-4.9	17.9	7.4×10^{-6} [4.8×10^{-6} to 5.7×10^{-5}]
Indomalaya	2 626 474	31.6	-28.3	59.9	2.3×10^{-5} [1.5×10^{-5} to 2.1×10^{-4}]
Palearctic	4 221 663	5.8	-4.3	10.1	2.4×10^{-6} [7.6×10^{-8} to 2.3×10^{-5}]
Nearctic	4 606 898	31.6	-17.4	48.9	1.1×10^{-5} [7.1×10^{-6} to 6.2×10^{-5}]
Australasia	1 088 250	1.9	-4.8	6.6	6.1×10^{-6} [8.3×10^{-7} to 5.4×10^{-5}]
China	1 141 180	16.6	-10.1	26.7	2.3×10^{-5} [1.7×10^{-5} to 2.3×10^{-4}]
Amazon	6 775 429	96.2	-394.0	490.2	7.2×10^{-5} [4.5×10^{-5} to 2.0×10^{-4}]
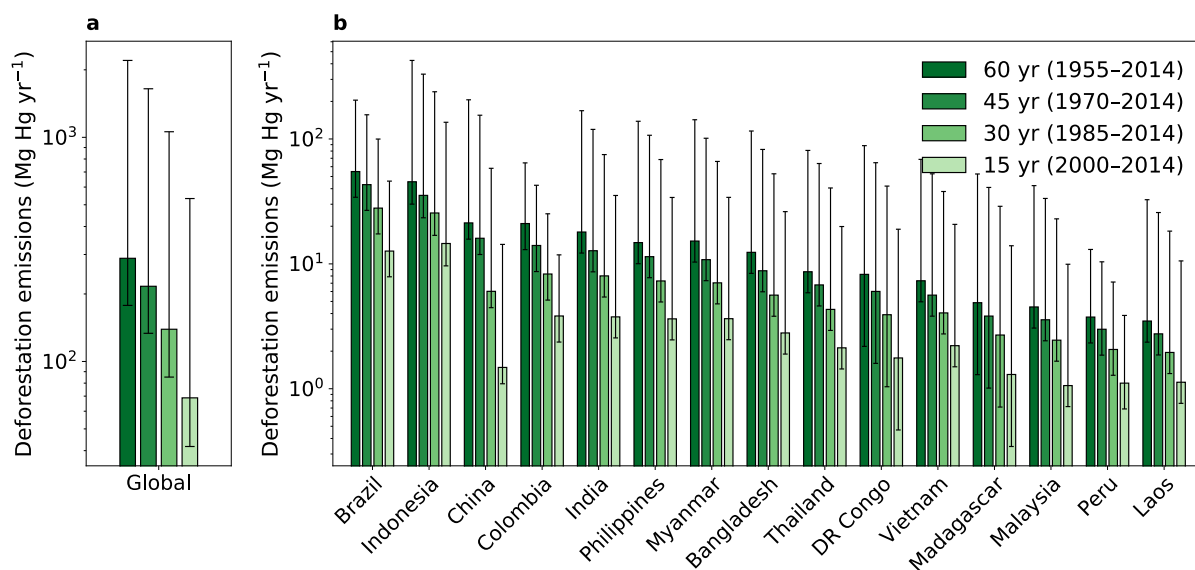
187

188 **Figure S7**. **a.** Global and **b.** country-level deforestation emissions of Hg for the top 15 emitting
189 countries. Results are summarized accumulating deforested area over different time horizons (15
190 years, 30 years, 45 years, and 60 years) before 2015. Error bars refer to the 95% confidence interval
191 based on the uncertainty in model parameters (Section S4).
192
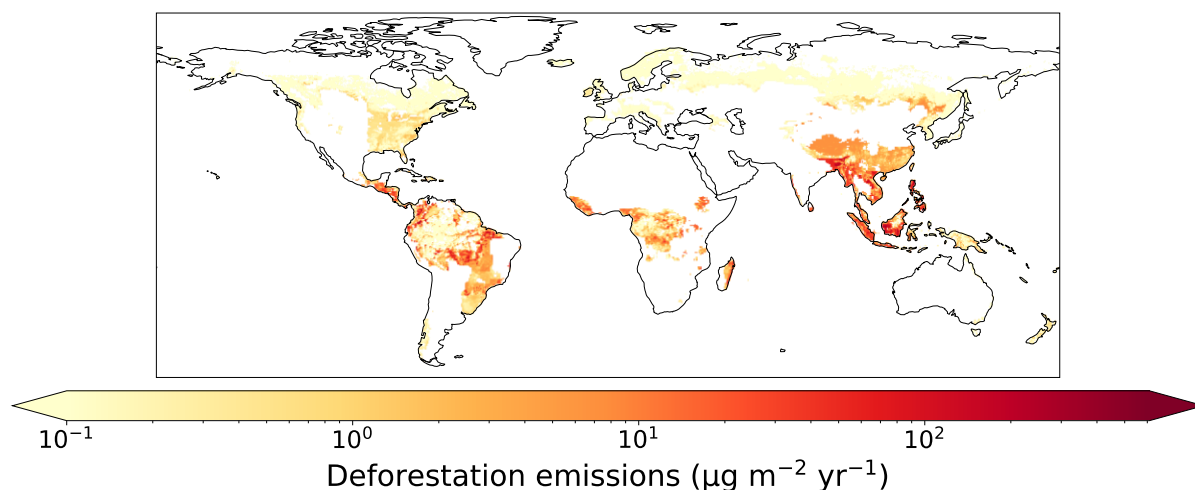
193

194 **Figure S8**. Map of net emissions of Hg from deforestation calculated over a 45 year time horizon
195 before 2015 (1970–2014), using deforested area from the LUH2 dataset[32].
196

197

Section S4. Parameters used in uncertainty analysis

Table S4. Parameter uncertainty bounds applied in the uncertainty analysis.

| Parameter	Min	Max	Units	Distribution	Comment
Soil emission parametrization	1	100	-	Uniform	Integer representing one of 100 reasonable parametrizations calculated within the range of observed uncertainties (Table S5)
Percentile of replaced LAI when building scenarios	10	90	-	Uniform	e.g., deforested Amazon area is assigned 10th percentile LAI of HIST savanna, instead of mean for default estimate
Dry deposition Hg^0 reactivity (f_0) Amazon rainforest	10^{-2}	0.5	-	Loguniform	Based on Feinberg et al.[31], within range of available vegetation uptake measurements
Dry deposition Hg^0 reactivity (f_0) other rainforests	10^{-5}	0.2	-	Loguniform	Based on Feinberg et al.[31]; no available measurements from other rainforests, leading to wider f_0 uncertainty
Dry deposition Hg^0 reactivity (f_0) elsewhere	10^{-5}	5×10^{-5}	-	Uniform	Based on Feinberg et al.[31], within range of available vegetation uptake measurements
Biomass burning emission factor for Amazon	350	615	$\mu g\ m^{-2}$	Uniform	Estimated range in literature[10,33,34]

Table S5. Bounds of observed parameters used to calculate 100 reasonable soil emission parametrizations, which are then applied in the uncertainty analysis (Table S4).

| Parameter	Min	Max	Units	Comment
Ratio of deforested to forested Amazon soil emissions	1.8	31	-	Range from Table S1
Ratio of Amazon to extratropical soil emissions	3.5	8	-	Assume 50% error from Table S2
Extratropical grassland soil emissions	3.5	11.4	$\mu g\ m^{-2}\ yr^{-1}$	Grasslands and background soil range from literature reviews[6,7]
Deforested Amazon soil emissions	9.8	79	$\mu g\ m^{-2}\ yr^{-1}$	Range from Table S1

206 **Section S5. Scenarios for Amazon deforestation and global reforestation**
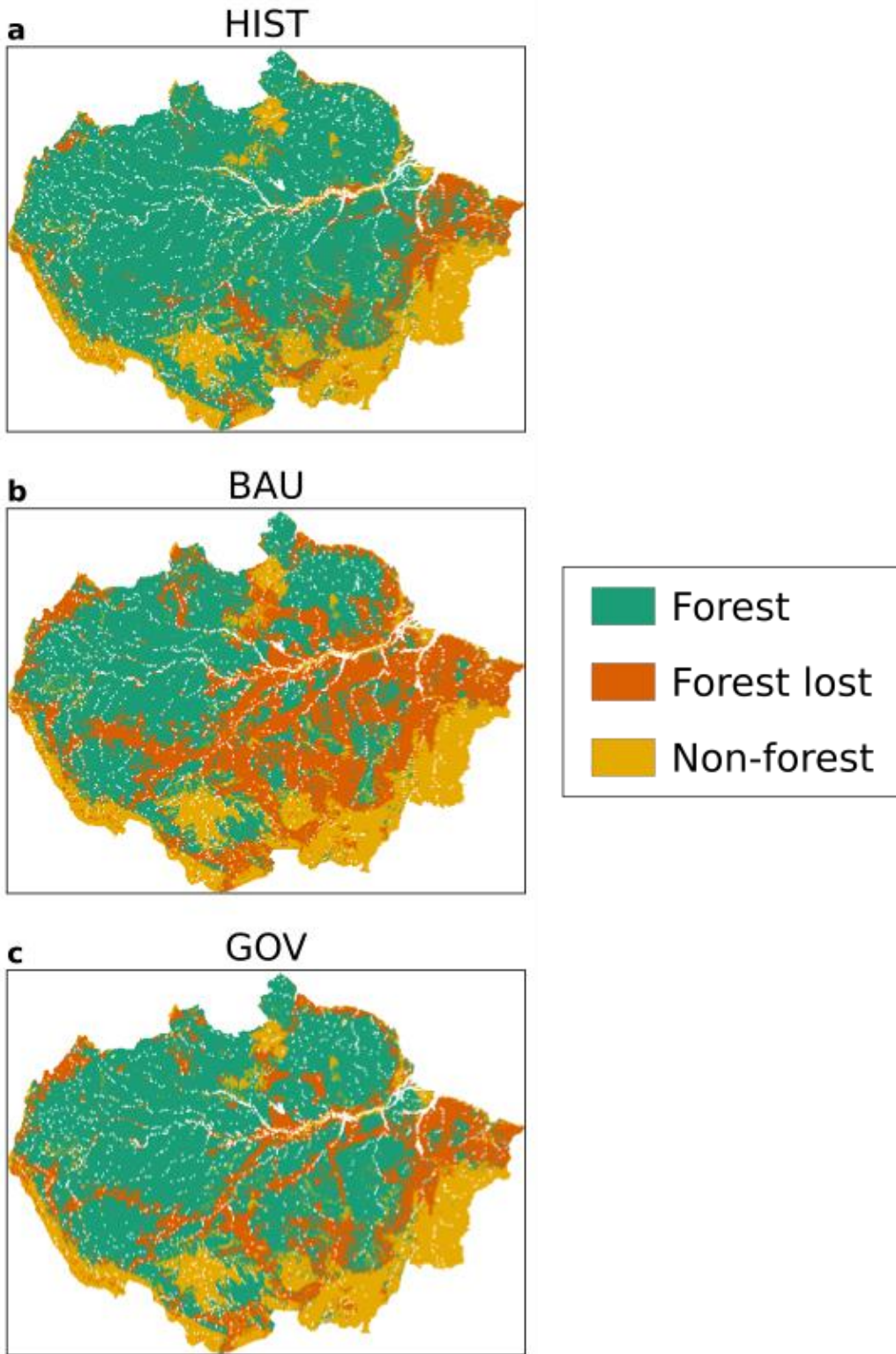
207

208 **Figure S9.** Map of the Amazon basin showing the area of forest, forest loss and rangeland and
209 agriculture in **a.** HIST; and projections for 2050 in **b**. Business as Usual (BAU) and **c.** Governance
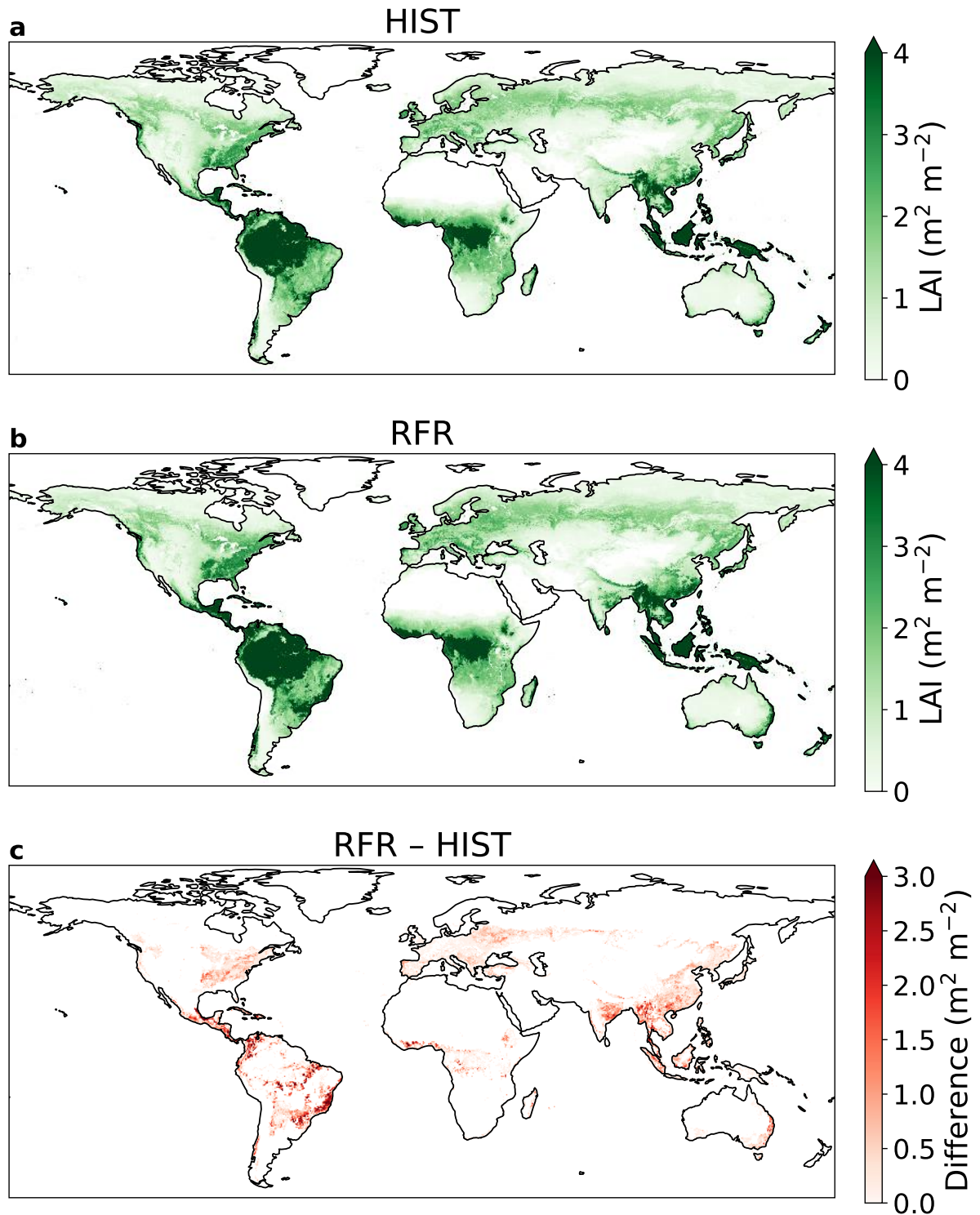210 (GOV) scenarios (replotted from Soares-Filho et al.[35] data).

211

212

213
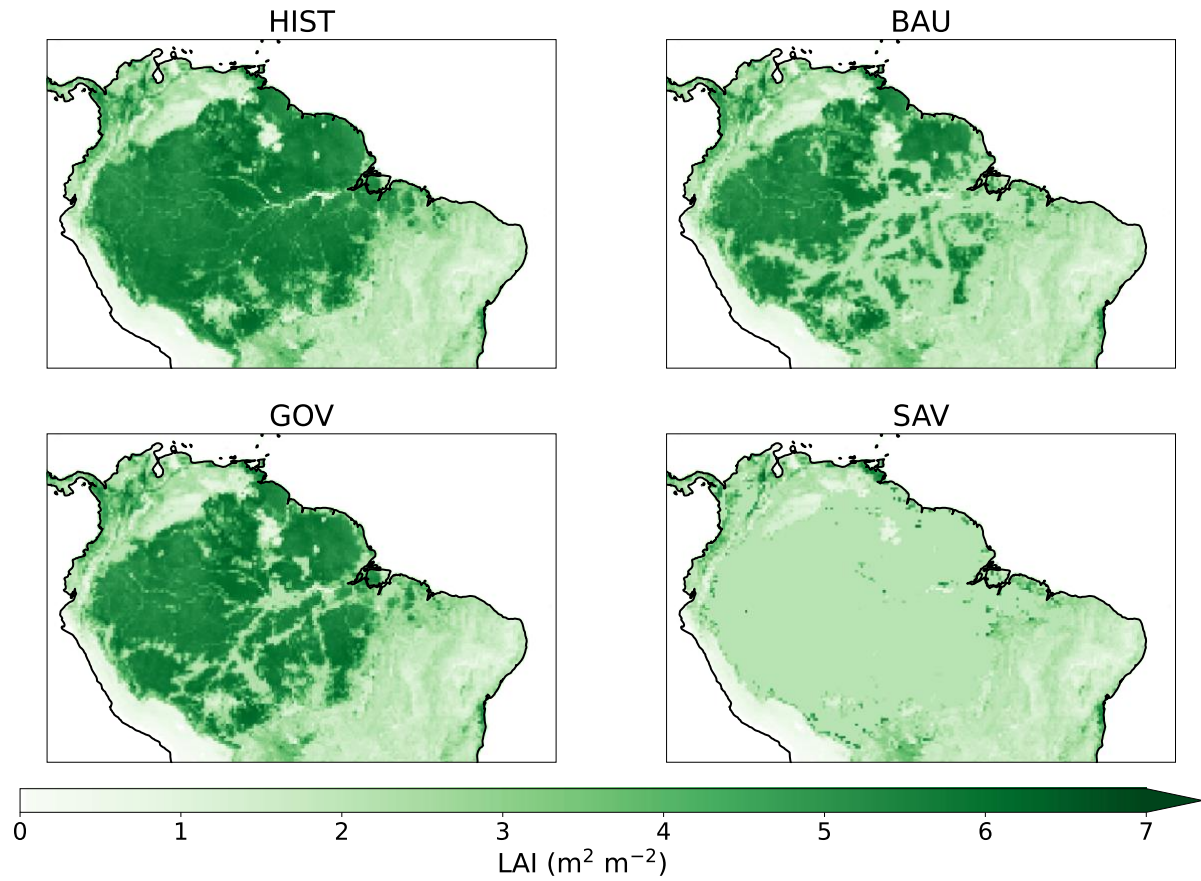
Figure S10. Annual mean leaf area index (LAI) maps for the Amazon deforestation scenarios at 0.25°
× 0.25° resolution. The simulations names refer to the following scenarios: reference (HIST),
Business-as-usual (BAU), Governance (GOV), and Savannization (SAV).

Figure S11. Annual mean leaf area index (LAI) maps at $0.25 \times 0.25°$ resolution for: **a.** the reference (HIST) scenario **b.** Reforestation scenario (RFR) **c.** Difference between RFR and HIST.

Section S6. Impact of Amazon deforestation on erosion

Previous field studies[15,36] have suggested that erosion of Hg is increased after deforestation in the Amazon, measuring enhanced runoff of Hg in deforested catchments. We estimated the change in soil displacement by water erosion (soil erosion) in the Amazon deforestation

225   scenarios using the RUSLE-based[37] modeling platform Global Soil Erosion Modeling

226   (GloSEM)[38,39]. As a detachment-limited soil erosion prediction model, GloSEM estimates soil

227   erosion (expressed as a mass of soil lost per unit area and time, Mg ha^{-1} yr^{-1}) due to inter-rill

228   and rill erosion processes by multiplication of six contributing factors. The modeling scheme

229   follows the same principle of most RUSLE-type models or more complex catchment-scale

230   process-based models, with a driving force (erosivity of the climate, R), a resistance term

231   (erodibility of the soil, K) and other factors representing the farming choice, i.e.,

232   topographical conformation of the field (LS), cropping system (C), and soil conservation

233   practices (P).

234   Our approach for calculating soil erosion in the Amazon scenarios is similar to the

235   GloSEM parametrization adopted by Borrelli et al.[38,39] to estimate human-induced soil erosion

236   change between 2001 and 2070 at a global scale. The horizontal resolution of the native soil

237   erosion modeling is 250×250 m. The calculation of erosivity (R), erodiblity (K),

238   topographical conformation of the field (LS), and soil conservation practices (P) factors are

239   described in Borrelli et al.[38,39]. We acknowledge that the calculation of erosion model factors

240   for the Amazon rainforest may be associated with higher uncertainties than other regions due

241   to the lower density in meteorological stations[40] and soil sampling sites[41]. For this study, we

242   adapted the computation of the land cover and management factor (C-factor), which measures

243   the combined effect of vegetation cover and cropping system variables on the soil erosion

244   process. We parametrize the C-factor according to two layers of information: 1) the spatial

245   dimension of land use classes according to the deforestation scenarios from Soares-Filho et

246   al.[35] (described below); 2) the vegetation condition in each land use class using the MODIS

247   MOD44B Vegetation Continuous Fields product (VCF) (~250m spatial resolution) as a proxy

248   to quantify (i) surface vegetation cover, (ii) tree cover, and (iii) bare soil. As we focus our

249   analysis on comparing the forest coverage in the years 2003 and 2050, the baseline vegetation

250   condition is given by the average VCF values over the years 2000, 2001 and 2002. The C-

251   factor for noncropland areas (C_{nc}) is estimated in two steps. First, a preliminary C-factor (C_p)

252   not considering tree cover is calculated as:

253    $$C_p = C_{min} + \left((C_{max} - C_{min})\, \text{NVS} \right) \qquad \text{(S6)}$$

254   where the C_{min} (0.01) and C_{max} (0.15) express the potential range in C-factor values for

255   dense to sparse grassland cover. NVS (non-vegetated surface) is spatially defined using the

256   MODIS MOD44B VCF data normalized to a range from 0 to 1 and describes the percentage

257   of ground covered by any vegetation type. For the NVS, the C-factor is set to 0.5. Within the

258   next step, the final land cover and management C-factor for non-croplands (C_{nc}) is computed

259 including the tree coverage (TC) defined using the MODIS MOD44B VCF normalized to

260 range from 0 to 1:

261
$$C_{nc} = C_{p\,min} + \left(\left(C_{p\,max} - C_{p\,min} \right) \mathrm{TC} \right) \quad \text{(S7)}$$

262 where the $C_{p\,min}$ and $C_{p\,max}$ values are set to 0.0001 (100% canopy cover) and 0.009 (sparse

263 forest vegetation).

264 While the deforestation scenarios proposed by Soares-Filho et al.[35] provide a spatial

265 quantification of the forest losses between 2003 and 2050, the annual shares of conversion

266 from forest to grassland or cropland are separate from the annual projection of the Land-Use

267 Harmonization (LUH2) data[32], which provides fractional land-use patterns (850-2100) at

268 $0.25° \times 0.25°$ resolution. The downscaling of the LUH2 fractional cropland and grassland

269 data from $0.25° \times 0.25°$ resolution to the 250 m $\times$ 250 m resolution of the erosion model is

270 performed through a probabilistic land use allocation scheme based on classification rules

271 applied to auxiliary information (i.e., a crop suitability index, more detail in Borrelli et al.[38]).

272 Finally, the C-factor of the cropland is defined at sub-national administrative level (Global

273 Administrative Unit Levels) based on the Food and Agriculture Organization's (FAO)

274 FAOSTAT database, which allowed to statistically describe typical crop rotations in each

275 region. The C-factor of the croplands ranges from 0.131 (Northern Suriname) to 0.332

276 (Northeast Brazil).

277 Following the assumption of Lugato et al.[42] for eroded carbon, we assume that 30% of

278 the eroded soil flux is not redeposited on land and enters riverine systems. The fraction of

279 eroded Hg which enters aquatic systems is uncertain, depending on hillslopes dynamics and

280 flow patterns that are not explicitly modeled by the RUSLE-based framework, as well as

281 whether Hg would be selectively eroded relative to carbon. We recognize that this assumption

282 introduces uncertainty into our calculations, and assume that the fraction of eroded soil which

283 enters riverine systems can vary between 5–47%, the range reported by Van Oost et al.[43] We

284 calculate the eroded flux of Hg from land by multiplying the soil flux by the median Hg

285 concentration in Amazon forested soils from a literature review (86 ng g^{-1}; see SI

286 Spreadsheet).

287 For each Amazon scenario, we tabulate the Hg erosion fluxes in Table S6. Erosion in

288 the HIST scenario represents a flux of 64 Mg yr^{-1} (uncertainty range: 11–100 Mg yr^{-1}).

289 Erosion is enhanced in the deforestation scenarios, ranging from +14% increase in GOV to a

290 96% increase in the extreme SAV scenario. The absolute magnitudes of erosion flux changes

291 are smaller than the perturbations in the land-air flux, driven by changes in Hg^0 soil emissions

292 and dry deposition (Table S6). Overall, perturbations to the erosion flux are approximately

293   14% of the perturbations to the land-air flux due to deforestation. A previous field study[5] has

294   also suggested that the majority of flux changes after deforestation occurs through

295   atmospheric exchange (97%) rather than erosion to riverine systems. Therefore, the land-air

296   changes to the fluxes play the larger role in the impact of deforestation on the mass balance of

297   Hg in soils. Nevertheless, changes to erosion will affect downstream Hg concentrations and

298   the methylation potential after deforestation[5,29], which would be important to consider when

299   assessing the impact of deforestation on local ecosystems.

300

301   **Table S6**. Soil erosion fluxes for the Amazon basin calculated by the erosion model GloSEM. The
302   simulations names refer to the following scenarios: reference (HIST), Business-as-usual (BAU),
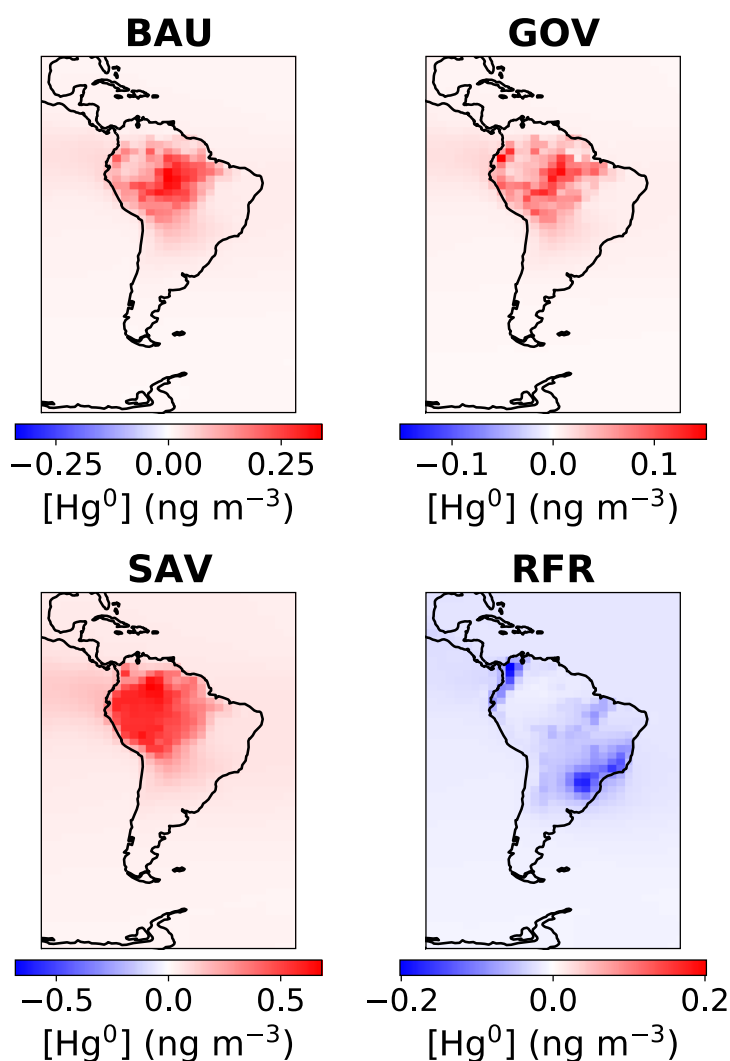303   Governance (GOV), and Savannization (SAV).

Scenario	HIST	BAU	GOV	SAV
Soil loss (Mt yr^{-1})	2467	3276	2816	4834
30% of soil loss (Mt yr^{-1})^a	740	983	845	1450
[5%–47%]	[123–1159]	[164–1540]	[141–1323]	[242–2272]
Hg erosion (Mg yr^{-1})	64	85	73	125
[uncertainty range]	[11–100]	[14–132]	[12–114]	[21–195]
Change from HIST (Mg yr^{-1})	-	21	9	61
(relative change)		(+33%)	(+14%)	(+96%)
Land-air flux change from HIST (Mg yr^{-1})	-	153	61	441

304   ^{a} This is the flux assumed to be entering riverine systems

305

306

307 **Section S7. Impacts on atmospheric Hg concentrations**

308

309 **Figure S12.** Annual mean differences in simulated atmospheric Hg^0 concentration at the surface
310 between scenarios — Business-as-usual (BAU), Governance (GOV), Savannization (SAV), and global
311 reforestation (RFR) — and the HIST reference simulation.

312

313 **Supplementary References**

314 1. Khan, T. R., Obrist, D., Agnan, Y., Selin, N. E. & Perlinger, J. A. Atmosphere-terrestrial
315 exchange of gaseous elemental mercury: parameterization improvement through direct
316 comparison with measured ecosystem fluxes. *Environ. Sci.: Processes Impacts* **21**, 1699–
317 1712 (2019).
318 2. Selin, N. E. *et al.* Global 3-D land-ocean-atmosphere model for mercury: Present-day
319 versus preindustrial cycles and anthropogenic enrichment factors for deposition. *Global
320 Biogeochem. Cycles* **22**, GB2011 (2008).
321 3. Verstraete, M. M. Radiation transfer in plant canopies: Transmission of direct solar
322 radiation and the role of leaf orientation. *J. Geophys. Res.* **92**, 10985 (1987).
323 4. Zhou, J., Wang, Z., Zhang, X., Driscoll, C. T. & Lin, C.-J. Soil–atmosphere exchange flux
324 of total gaseous mercury (TGM) at subtropical and temperate forest catchments. *Atmos.
325 Chem. Phys.* **20**, 16117–16133 (2020).

5. Eckley, C. S., Eagles-Smith, C., Tate, M. T. & Krabbenhoft, D. P. Surface-air mercury fluxes and a watershed mass balance in forested and harvested catchments. *Environmental Pollution* **277**, 116869 (2021).

6. Zhu, W. *et al.* Global observations and modeling of atmosphere–surface exchange of elemental mercury: a critical review. *Atmos. Chem. Phys.* **16**, 4451–4480 (2016).

7. Agnan, Y., Le Dantec, T., Moore, C. W., Edwards, G. C. & Obrist, D. New Constraints on Terrestrial Surface–Atmosphere Fluxes of Gaseous Elemental Mercury Using a Global Database. *Environ. Sci. Technol.* **50**, 507–524 (2016).

8. Magarelli, G. & Fostier, A. Influence of deforestation on the mercury air/soil exchange in the Negro River Basin, Amazon. *Atmos. Environ.* **39**, 7518–7528 (2005).

9. Almeida, M. D., Marins, R. V., Paraquetti, H. H. M., Bastos, W. R. & Lacerda, L. D. Mercury degassing from forested and open field soils in Rondônia, Western Amazon, Brazil. *Chemosphere* **77**, 60–66 (2009).

10. Carpi, A., Fostier, A. H., Orta, O. R., dos Santos, J. C. & Gittings, M. Gaseous mercury emissions from soil following forest loss and land use changes: Field experiments in the United States and Brazil. *Atmos. Environ.* **96**, 423–429 (2014).

11. Song, S. *et al.* Top-down constraints on atmospheric mercury emissions and implications for global biogeochemical cycling. *Atmos. Chem. Phys.* **15**, 7103–7125 (2015).

12. Horowitz, H. M. *et al.* A new mechanism for atmospheric mercury redox chemistry: implications for the global mercury budget. *Atmos. Chem. Phys.* **17**, 6353–6371 (2017).

13. Gamby, R. L., Hammerschmidt, C. R., Costello, D. M., Lamborg, C. H. & Runkle, J. R. Deforestation and cultivation mobilize mercury from topsoil. *Science of The Total Environment* **532**, 467–473 (2015).

14. Homann, P. S., Darbyshire, R. L., Bormann, B. T. & Morrissette, B. A. Forest Structure Affects Soil Mercury Losses in the Presence and Absence of Wildfire. *Environ. Sci. Technol.* **49**, 12714–12722 (2015).

15. Fostier, A. H. *et al.* Mercury fluxes in a natural forested Amazonian catchment (Serra do Navio, Amapá State, Brazil). *Sci. Total Environ.* **260**, 201–211 (2000).

16. Gerson, J. R. *et al.* Amazon forests capture high levels of atmospheric mercury pollution from artisanal gold mining. *Nat Commun* **13**, 559 (2022).

17. Almeida, M. D., Lacerda, L. D., Bastos, W. R. & Herrmann, J. C. Mercury loss from soils following conversion from forest to pasture in Rondônia, Western Amazon, Brazil. *Environmental Pollution* **137**, 179–186 (2005).

18. Lacerda, L. D., de Souza, M. & Ribeiro, M. G. The effects of land use change on mercury distribution in soils of Alta Floresta, Southern Amazon. *Environmental Pollution* **129**, 247–255 (2004).

19. Béliveau, A., Lucotte, M., Davidson, R., do Canto Lopes, L. O. & Paquet, S. Early Hg mobility in cultivated tropical soils one year after slash-and-burn of the primary forest, in the Brazilian Amazon. *Science of The Total Environment* **407**, 4480–4489 (2009).

20. Béliveau, A. *et al.* Reduction of soil erosion and mercury losses in agroforestry systems compared to forests and cultivated fields in the Brazilian Amazon. *Journal of Environmental Management* **203**, 522–532 (2017).

21. Patry, C., Davidson, R., Lucotte, M. & Béliveau, A. Impact of forested fallows on fertility and mercury content in soils of the Tapajós River region, Brazilian Amazon. *Science of The Total Environment* **458–460**, 228–237 (2013).

22. Comte, I. *et al.* Impacts of Land Uses on Mercury Retention in Long-Time Cultivated Soils, Brazilian Amazon. *Water Air Soil Pollut* **224**, 1515 (2013).

23. Mainville, N. *et al.* Decrease of soil fertility and release of mercury following deforestation in the Andean Amazon, Napo River Valley, Ecuador. *Science of The Total Environment* **368**, 88–98 (2006).

376 24. Roulet, M. *et al.* The geochemistry of mercury in central Amazonian soils developed on
377 the Alter-do-Chão formation of the lower Tapajós River Valley, Pará state, Brazil.
378 *Science of The Total Environment* **223**, 1–24 (1998).
379 25. Wasserman, J. C., Campos, R. C., Hacon, S. de S., Farias, R. A. & Caires, S. M. Mercury
380 in soils and sediments from gold mining liabilities in Southern Amazonia. *Quím. Nova* **30**,
381 (2007).
382 26. Wang, X. *et al.* Emission-dominated gas exchange of elemental mercury vapor over
383 natural surfaces in China. *Atmos. Chem. Phys.* **16**, 11125–11143 (2016).
384 27. Mazur, M. *et al.* Gaseous mercury fluxes from forest soils in response to forest harvesting
385 intensity: A field manipulation experiment. *Science of The Total Environment* **496**, 678–
386 687 (2014).
387 28. Ma, M., Wang, D., Sun, R., Shen, Y. & Huang, L. Gaseous mercury emissions from
388 subtropical forested and open field soils in a national nature reserve, southwest China.
389 *Atmospheric Environment* **64**, 116–123 (2013).
390 29. Eklöf, K., Lidskog, R. & Bishop, K. Managing Swedish forestry's impact on mercury in
391 fish: Defining the impact and mitigation measures. *Ambio* **45**, 163–174 (2016).
392 30. De Wit, H. A. *et al.* Forest harvest effects on mercury in streams and biota in Norwegian
393 boreal catchments. *Forest Ecology and Management* **324**, 52–63 (2014).
394 31. Feinberg, A., Dlamini, T., Jiskra, M., Shah, V. & Selin, N. E. Evaluating atmospheric
395 mercury (Hg) uptake by vegetation in a chemistry-transport model. *Environ. Sci.:*
396 *Processes Impacts* **24**, 1303–1318 (2022).
397 32. Hurtt, G. C. *et al.* Harmonization of global land use change and management for the
398 period 850–2100 (LUH2) for CMIP6. *Geosci. Model Dev.* **13**, 5425–5464 (2020).
399 33. Michelazzo, P. A. M., Fostier, A. H., Magarelli, G., Santos, J. C. & de Carvalho, J. A.
400 Mercury emissions from forest burning in southern Amazon. *Geophys. Res. Lett.* **37**,
401 L09809 (2010).
402 34. Melendez-Perez, J. J. *et al.* Soil and biomass mercury emissions during a prescribed fire
403 in the Amazonian rain forest. *Atmospheric Environment* **96**, 415–422 (2014).
404 35. Soares-Filho, B. S. *et al.* Modelling conservation in the Amazon basin. *Nature* **440**, 520–
405 523 (2006).
406 36. Roulet, M. *et al.* Effects of Recent Human Colonization on the Presence of Mercury in
407 Amazonian Ecosystems. *Water Air Soil Pollut.* **112**, 297–313 (1999).
408 37. Renard, K. G., Foster, G. R., Weesies, G. A., McCool, D. K. & Yoder, D. C. Predicting
409 soil erosion by water: A guide to conservation planning with the Revised Universal Soil
410 Loss Equation (RUSLE). *Agriculture handbook* **703**, (1997).
411 38. Borrelli, P. *et al.* Land use and climate change impacts on global soil erosion by water
412 (2015-2070). *Proc. Natl. Acad. Sci. U.S.A.* **117**, 21994–22001 (2020).
413 39. Borrelli, P. *et al.* An assessment of the global impact of 21st century land use change on
414 soil erosion. *Nat Commun* **8**, 2013 (2017).
415 40. Panagos, P. *et al.* Global rainfall erosivity assessment based on high-temporal resolution
416 rainfall records. *Sci Rep* **7**, 4175 (2017).
417 41. Hengl, T. *et al.* SoilGrids1km — Global Soil Information Based on Automated Mapping.
418 *PLoS ONE* **9**, e105992 (2014).
419 42. Lugato, E. *et al.* Soil erosion is unlikely to drive a future carbon sink in Europe. *Sci. Adv.*
420 **4**, eaau3523 (2018).
421 43. Van Oost, K. *et al.* The Impact of Agricultural Soil Erosion on the Global Carbon Cycle.
422 *Science* **318**, 626–629 (2007).
423